SILICON NITRIDE MICRORESONATORS AT 1.06 MICRONS

A Dissertation

Submitted to the Faculty

of

Purdue University

by

Eric J. Topel

In Partial Fulfillment of the

Requirements for the Degree

of

Master of Science in Electrical and Computer Engineering

May 2017

Purdue University

West Lafayette, Indiana

THE PURDUE UNIVERSITY GRADUATE SCHOOL
STATEMENT OF DISSERTATION APPROVAL

Dr. Andrew Weiner, Chair

School of Electrical and Computer Engineering

Dr. Minghao Qi

School of Electrical and Computer Engineering

Dr. Tongcang Li

Department of Physics and Astronomy

Approved by:

Dr. Venkataramanan Balakrishnan

Head of the School Graduate Program

ACKNOWLEDGMENTS

A great many people helped in making this work possible. Chief among them is Prof. Andrew M. Weiner, who provided continuous instruction and guidance while pushing me and the other members of his lab to be the best researchers, collaborators, and communicators of science we can be. Acknowledgement is also due to my other committee members: Prof. Minghao Qi, whose collaboration is invaluable to our group, and Prof. Tongcang Li, whose course on optics broadened my perspective on the field. Special thanks also to Dr. Dan Leaird, without whose technical and logistical wizardry the lab could not run.

A number of current and former graduate students also made substantial contributions to this research and my education at Purdue. I would particularly like to mention Dr. Pei-Hsun Wang, who gave me my first introduction to this field; Dr. Chengying Bao, for advice and guidance; Kyunghun Han, for fabricating many of the devices used in this work; and Yun Jo Lee, for providing SEM images and analysis. Thank you also to the other members of Prof. Weiner's and Prof. Qi's groups for being talented and supportive coworkers these past two years.

Last but not least, I would like to thank my parents and my girlfriend, Sonja, for their constant love, encouragement, and inspiration. A big thank you also to the entire team at Greyhouse Coffee & Supply, without whom this thesis would almost certainly not have been finished on time.

TABLE OF CONTENTS

Page

LIST OF TABLES

LIST OF FIGURES

Figure Page

Figure Page

SYMBOLS

A_{eff}	Effective mode area
β	Propagation constant
D	Dispersion parameter
D_m	Asymmetry factor
γ	Kerr coefficient
K	Coupling parameter
κ	Mode coupling coefficient
κ_e^2	Coupling loss per round trip
κ_p^2	Intrinsic loss per round trip
n_2	Nonlinear refractive index
n_g	Group refractive index
P_{th}	Threshold power for comb
Q	Quality factor
T	Transmittance
t_R	Round-trip time

ABBREVIATIONS

CMOS	Complementary metal-oxide-semiconductor
CW	Continuous wave
FSR	Free spectral range
FWM	Four-wave mixing
GVD	Group velocity dispersion
HSQ	Hydrogen silsesquioxane
KLM	Kerr-lens mode-locking
LPCVD	Low-pressure chemical vapor deposition
MI	Modulation instability
OSA	Optical spectrum analyzer
PC	Polarization controller
PM	Polarization-maintaining or power meter
Si_3N_4	Silicon nitride
TE	Transverse electric
TLS	Tunable laser source
TM	Transverse magnetic
WLM	Wavelength meter
YDFA	Ytterbium-doped fiber amplifier

ABSTRACT

Topel, Eric J. M.S.E.C.E, Purdue University, May 2017. Silicon nitride microresonators at 1.06 microns. Major Professor: Andrew M. Weiner.

Optical frequency combs have numerous applications in spectroscopy, metrology, and communications. Silicon nitride microresonators can produce broadband combs with lower cost, smaller physical footprint, and higher repetition rate than current commercial technologies, but most previous work on this platform has been done with pump wavelengths around 1.55 μm. The availability of equipment operating at 1.06 μm makes this an attractive wavelength for expanding the functionality of Si_3N_4 resonators. However, comb generation is complicated by stronger normal dispersion, lower quality factors, and waveguide damage at high optical power. This thesis explores device design and experimental methods for navigating these challenges. Waveguide dispersion engineering is investigated using finite element simulation and in practice. Evidence of transverse mode coupling at 1 micron, which can be used to generate normal dispersion combs, is also presented. A free-space pump blocking setup for easier detection of comb power is demonstrated. Finally, thermally-induced tensile strain and the fiber fuse effect are identified as the mechanisms behind high power damage, and suggestions are made for their mitigation.

1. INTRODUCTION

Optical frequency combs are, simply put, spectra consisting of sharp, equally-spaced lines. They can function as a precise "optical ruler" for spectroscopy and metrology [1]. Optical clocks based on frequency combs have exceeded the accuracy of the best cesium atomic clocks by more than two orders of magnitude [2]. They are also used, in the form of mode-locked lasers, to produce femtosecond-scale optical pulses that have opened up new frontiers in time-resolved spectroscopy and arbitrary waveform synthesis [3] [4].

Clearly, expanding the functionality and lowering the cost of frequency combs is a worthwhile enterprise. While mode-locked lasers have made great strides in recent years, they are still generally expensive and have practical limits on their repetition rate [5]. For these reasons, comb generation through cascaded four-wave mixing in optical microresonators has become an active area of research. Although a number of resonator designs have been successfully demonstrated, planar silicon nitride (Si_3N_4) has the advantage of being CMOS-compatible [6].

The majority of work on silicon-nitride microresonators has been done in the C band of the infrared (1530-1565 nm) due to its wide use in telecommunications and the easy availability of equipment, including erbium-doped fiber amplifiers to generate the high power needed for comb generation. However, to achieve wider applicability, it is necessary to expand the wavelength range available for use with this technology. The territory of 1060 nm is a good place to begin given the commercial availability of ytterbium-doped fiber amplifiers and f-2f stabilization technology in this range, as well as potential applications in astronomical spectroscopy [7]. This thesis will explore the possibilities and challenges associated with optical frequency comb generation in the 1-micron wavelength band.

The rest of this section lays out the theory of comb generation, restrictions on combs in normal group velocity dispersion, and the use of transverse mode interactions to circumvent these restrictions. Section 2 discusses how microresonator design affects threshold power, mode coupling likelihood, and comb bandwidth, as well as trade-offs between these parameters at 1 micron. Section 3 describes the experimental setups and methods used in this research, including Q-factor and dispersion measurement, mode coupling identification, and comb power detection. It also discusses the causes of high-power waveguide damage. Finally, Section 4 provides a summary and recommendations for further work.

1.1 Optical Frequency Combs

An ideal frequency comb can be characterized by only two quantities: the comb spacing f_r and the offset frequency f_0, with the individual modes given by $f_n = f_0 + n \times f_r$. If the components have a flat spectral phase, they add to form a train of short pulses in the time domain with repetition rate f_r and pulse length inversely proportional to the bandwidth Δf (Figure 1.1). This is referred to as mode locking. A nonzero f_0 causes the phase of the carrier wave with respect to the envelope to slip from pulse to pulse [8].

A number of techniques are currently used to generate frequency combs for practical applications. Among the simplest is the use of an RF phase modulator to generate sidebands from a continuous-wave (CW) laser [9]. The current state of the art in short pulse generation is Kerr-lens mode-locking (KLM). The Kerr effect is a third-order nonlinearity in which the refractive index of a medium is intensity-dependent according to $n = n_0 + n_2 I$. The inclusion of a high-n_2 element allows a laser cavity to be designed which favors short, intense pulses over CW operation. Thus, a small variation in intracavity power will be reinforced to form a coherent frequency comb where f_r equals the inverse of the cavity round-trip time [10].

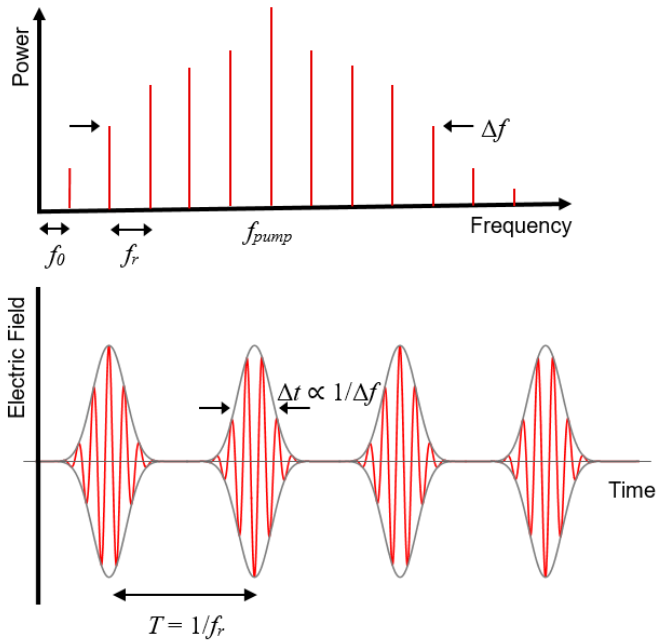

Fig. 1.1. A frequency comb and its time-domain pulse.

The mechanisms behind frequency comb generation in a microresonator are not dissimilar to those in a KLM laser. The resonator in question must have a large Kerr nonlinearity and evenly spaced modes with high quality factors (Q), a parameter representing the ratio of stored energy to energy lost per cycle. One of these modes is pumped with an external source, causing high-intensity CW light to build up inside the resonator. Noise in the input laser is reinforced by the nonlinearity in a process known as modulation instability (MI), which creates a region of gain around the pump wavelength [11].

If the gain spectrum overlaps with nearby resonator modes, power will begin to build up in these modes. Additional comb lines are then formed through cascaded four wave mixing (FWM), a related third-order nonlinear effect in which two photons of frequency ν_1 and ν_2 spaced $\Delta\nu$ apart are converted to one photon of frequency $\nu_1 - \Delta\nu$ and another of frequency $\nu_2 + \Delta\nu$. New lines will continue to form until dispersion causes the resonator modes to no longer overlap with the precise spacing

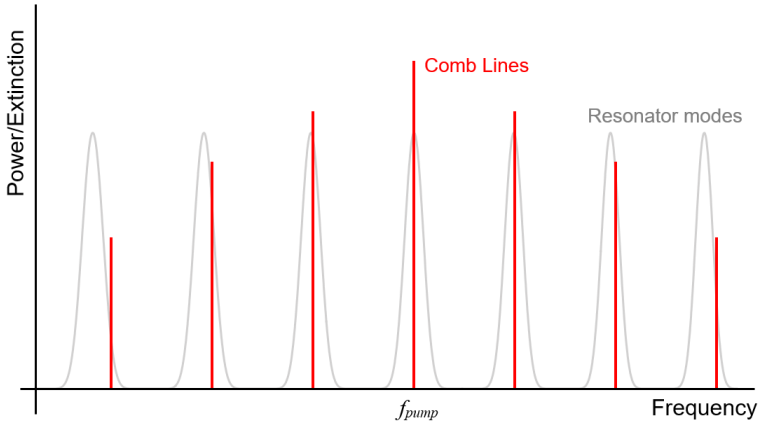

Fig. 1.2. The comb lines are spaced exactly, but the free spectral range of the resonator evolves due to dispersion. This degrades the FWM efficiency as one moves away from the pump wavelength.

of the comb (Figure 1.2) [8]. Unlike a KLM laser cavity, microresonators cannot easily be designed to favor short pulses. Therefore, the comb elements are not mode locked unless specific conditions for soliton formation are met [12].

Comb generation has been demonstrated in a number of microresonator designs and materials (Figure 1.3. The first studies were in silica toroids, which are notable for their high quality factors (on the order of 10^8) [13]. Other three-dimensional whispering gallery mode resonators have used fused quartz [14] or crystalline magnesium fluoride, which is well-suited to longer wavelengths [15]. Much recent work, however, has focused on planar ring resonators with an integrated input/output waveguide. Although these generally feature lower Q-factors (on the order of 10^6), they have the advantages of tighter optical field confinement and greater ease of fabrication [8]. Combs have been successfully produced using silicon [16], Hydex glass [11], and silicon nitride rings. The latter has proved especially popular due to its high nonlinear refractive index ($n_2 = 2.4 \times 10^{-15}$ cm^2/W) and large bandgap (5 eV), which prevents the two-photon absorption issues found in silicon waveguides [17] [18].

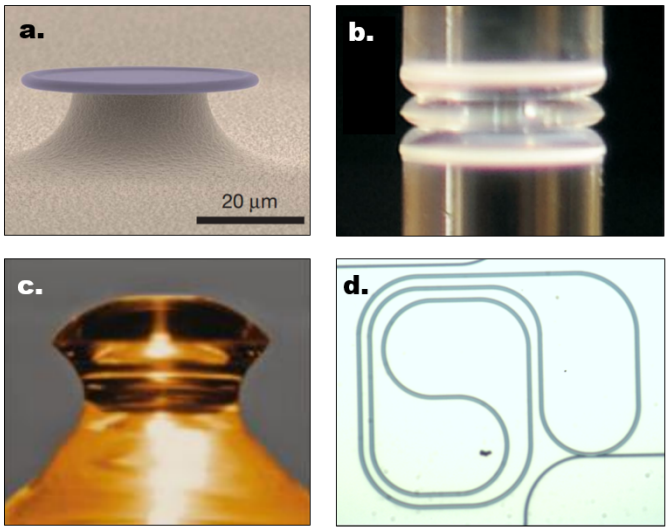

Fig. 1.3. Systems used for frequency comb generation. **(a)** Silica toroid on silicon chip [13] **(b)** Fused quartz rod. Resonant frequencies can be tuned through mechanical deformation [14] **(c)** Crystalline magnesium fluoride [15] **(d)** Silicon nitride waveguides on chip with oxide cladding, printed with e-beam lithography

1.2 Group Velocity Dispersion in Microresonators

One of the most important considerations for frequency comb generation in microresonators is group velocity dispersion (GVD), the dependence of the group velocity of light in a medium on frequency. The phase applied to light traveling through a waveguide of length L is given by

$$\phi = -\beta(\omega)L \tag{1.1}$$

where the propagation constant β equals the effective refractive index n_{eff} times the vacuum wavenumber $k_0 = 2\pi/\lambda$. Relative to some reference frequency ω_0, the Taylor expansion of this constant is

$$\beta(\omega) = \beta(\omega_0) + \frac{\partial\beta}{\partial\omega}(\omega - \omega_0) + \frac{1}{2}\frac{\partial^2\beta}{\partial\omega^2}(\omega - \omega_0)^2 + ... \tag{1.2}$$

The first-order dispersion, which also represents the inverse of the group velocity v_g, is given by $\beta_1 = \frac{\partial \beta}{\partial \omega}$. The GVD, or second-order dispersion, is given by $\beta_2 = \frac{d^2\beta}{d\omega^2}$. Optical pulses are composed of a range of frequencies, so GVD causes the pulse envelope to spread as it propagates. As this broadening effect is a major concern in optical communications, GVD is often represented by the dispersion parameter

$$D = -\frac{2\pi c}{\lambda^2}\beta_2 \tag{1.3}$$

with units of picoseconds of broadening per nanometer of bandwidth per kilometer of propagation length. When $D < 0$, higher frequency components propagate more slowly and pulses become up-chirped. This is referred to as normal dispersion, whereas cases where $D > 0$ are referred to as anomalous dispersion [19].

Group velocity dispersion has a significant impact on the phase-matching conditions for nonlinear optical effects. In order for the photons produced by these effects to add coherently along the length of the resonator waveguide, they must have a set phase relationship to the pump wave. This is expressed in terms of a phase mismatch $\Delta\beta$ to be minimized. For modulation instability at threshold, the phase mismatch is:

$$\Delta\beta = \beta_s + \beta_i - 2\beta_p + \gamma P \tag{1.4}$$

where β_p, β_s, and β_i are the propagation constants for the pump, signal, and idler, respectively. The last term represents nonlinear self- and cross-phase modulation: P is the pump power in the resonator and $\gamma = k_0 n_2 / A_{eff}$ is the Kerr coefficient of the waveguide, where A_{eff} is the effective mode area [20]. Conservation of energy requires that $2\nu_p = \nu_s + \nu_i$, so an additional effect is needed to cancel the nonlinear contribution to the phase.

We can examine the effects of dispersion by substituting Equation 1.2 into the phase mismatch expression, with the pump as the reference frequency and $\Delta\omega = \omega_s - \omega_p = \omega_p - \omega_i$:

$$\Delta\beta = (\beta_p + \beta_1\Delta\omega + \frac{1}{2}\beta_2\Delta\omega^2) + (\beta_p - \beta_1\Delta\omega + \frac{1}{2}\beta_2\Delta\omega^2) - 2\beta_p + \gamma P \tag{1.5}$$

$$\Delta\beta = \beta_2\Delta\omega^2 + \gamma P \tag{1.6}$$

If we set the phase mismatch equal to zero, we find that maximum MI gain is achieved when:

$$\Delta\omega^2 = -\frac{\gamma P}{\beta_2} \tag{1.7}$$

The full gain spectrum can be seen in Figure 1.4. Since Si_3N_4 has a positive γ, corresponding to a focusing Kerr nonlinearity, anomalous GVD is required to minimize the phase mismatch and allow for efficient MI. However, bulk silicon nitride has normal dispersion across most of the near infrared [21]. In the C band, where the normal dispersion is less than $D = -10$ ps/nm-km, it can be easily offset by waveguide effects. The region around 1060 nm, on the other hand, has dispersion of approximately -200 ps/nm-km. While it is possible to reach the anomalous regime through careful waveguide design [7], doing so requires trade-offs that will be discussed later in this thesis.

1.3 Mode Interactions and Normal-Dispersion Combs

While it is not possible for modulation instability to occur in a linear waveguide with normal dispersion, the use of a resonator opens up more options. A careful nonlinear Schrödinger equation analysis shows that MI can be achieved in normal dispersion by carefully controlling the pump detuning [23]. However, in practice this is difficult due to the strong resonant frequency shifts exhibited by microresonators at high power. Thermal expansion and the thermo-optic effect increase the optical path length as the pump laser is tuned into resonance [24].

Another solution comes from coupling between resonant modes. Rectangular waveguides of sufficient width can support multiple "families" of transverse modes

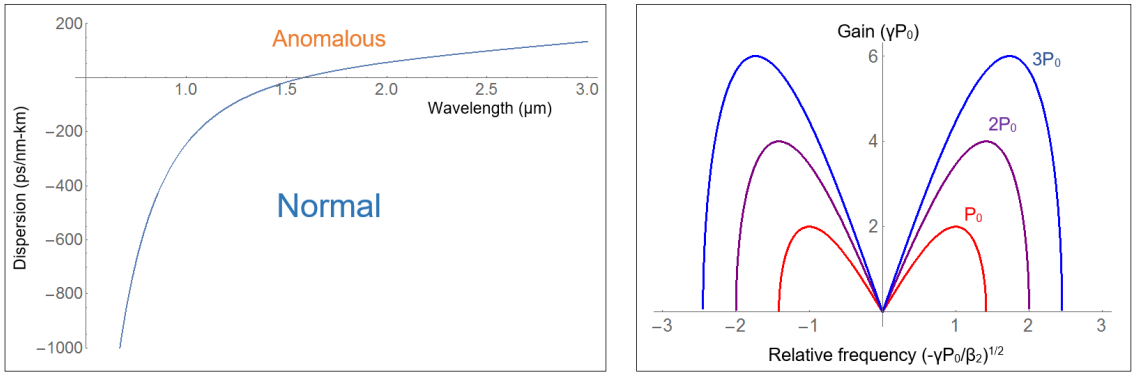

Fig. 1.4. **(a)** Material dispersion for silicon nitride, based on the Sellmeier equation from [21]. Changes from normal to anomalous at approximately 1.58 microns. **(b)** Normalized gain spectrum about the pump frequency for modulation instability. Based on analysis of the nonlinear Schrödinger equation [22].

for each polarization, each with a slightly different free spectral range (FSR). Eventually, these families will intersect in frequency space, and imperfections in the resonator can allow power to be coupled from one mode to another. The electric field in two nearby modes in response to low-power pumping can be modeled using the following differential equations [25]:

$$\frac{dE_1}{dt} = \left[-\frac{1}{\tau_{01}} - \frac{1}{\tau_{ex1}} - i(\omega_1 - \omega_p) \right] E_1 + i\kappa E_2 + \sqrt{\frac{2}{\tau_{ex1}}} E_p \tag{1.8}$$

$$\frac{dE_2}{dt} = \left[-\frac{1}{\tau_{02}} - \frac{1}{\tau_{ex2}} - i(\omega_2 - \omega_p) \right] E_2 + i\kappa E_1 + \sqrt{\frac{2}{\tau_{ex2}}} E_p \tag{1.9}$$

Here the $1/\tau_{0i}$ represent the decay rate of the field due to intrinsic loss, $1/\tau_{exi}$ the coupling rate between the resonator and bus waveguides, $\omega_i - \omega_p$ the detuning of the pump from resonance, and E_p the electric field of the pump in the bus waveguide. The strength of mode coupling is expressed in the coefficient κ. The effects of this coupling are most easily seen by examining the linear transmission spectrum of the

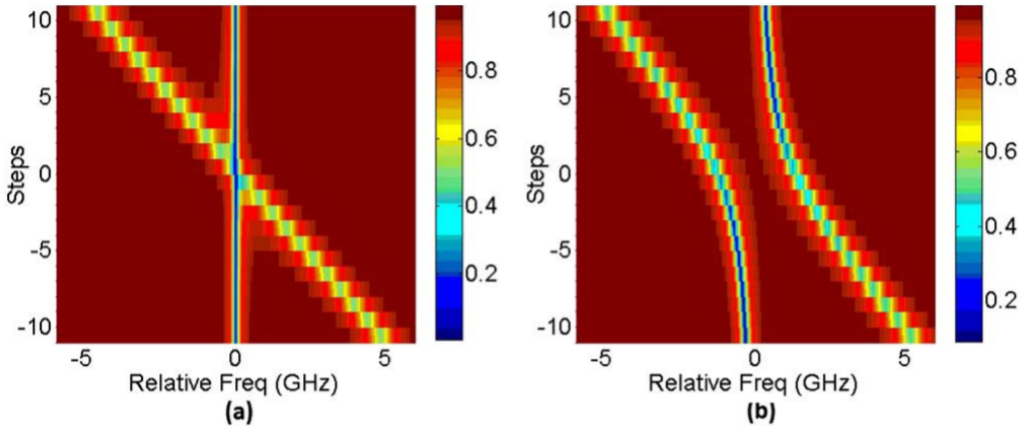

Fig. 1.5. Simulated microresonator mode crossings without **(a)** and with **(b)** mode coupling. Reproduced from [25].

resonator, or the power at the output of the bus waveguide as a low-power input laser sweeps through resonance. Normalized to input power, the transmission is given by:

$$T = \frac{\left|E_p - E_1\sqrt{2t_R/t_{ex1}} - E_2\sqrt{2t_R/t_{ex2}}\right|^2}{|E_p|^2} \tag{1.10}$$

where t_R is the resonator round-trip time [26]. Simulated transmission spectra with and without mode coupling are shown in Figure 1.5. Each row represents one FSR of the high-Q mode, which has a narrower dip in transmission. In the first case, where $\kappa = 0$, there is no interaction between the modes, and they cross without incident. In the second case, the nonzero κ coefficient means that one cannot stimulate one mode without some power being transfered to the other. This causes what is known in quantum mechanics as an avoided crossing: two states whose energy levels should cross as some parameter is varied instead become mixed near the intersection point, with state 'A' smoothly transitioning into state 'B' and vice versa [27]. In this case the parameter in question is the longitudinal mode number.

In optical terms, mode coupling causes a phase shift that changes the resonant frequency of the microring. In anomolous dispersion rings, this is generally undesirable, as it can increase the loss for some comb lines by shifting them out of res-

onance [28]. However, it can also create an effective local anomalous dispersion in normal-dispersion rings, allowing modulation instability gain and comb generation. As the pumped mode, the sidebands, or some combination thereof can be shifted depending on the position and strength of the avoided crossing, it is useful to define the asymmetry factor:

$$D_m = \omega_m - \omega_0 - (\omega_0 - \omega_{-m}) \tag{1.11}$$

where ω_0 is the pumped mode and $\omega_{\pm m}$ are the modes of the same family spaced m FSR away. This is related to the effective dispersion via [25]:

$$D_{eff} = \frac{n_{eff} D_m}{2\pi m^2 \lambda^2 \mathrm{FSR}^2} \tag{1.12}$$

Thus, a positive asymmetry factor for a trio of resonances is equivalent to anomalous local dispersion. It is important to note that these resonances need not be adjacent. If D_2 is positive but D_1 is negative, a comb with a spacing of $2 \cdot \mathrm{FSR}$ will be produced. Indeed, a potentially useful property of this method of comb generation is the ease with which multiple-FSR combs can be obtained, as the first sideband is "pinned" at the mode crossing wavelength [29].

Mode-coupling assisted comb generation also comes with drawbacks. First, the comb spectra tend to be asymmetric and limited in bandwidth due to higher-order dispersion associated with the avoided crossing [25]. Second, the presence of mode interactions in a desired wavelength range is largely a matter of luck. However, certain choices can be made in the design of the resonator to tilt the odds in our favor.

2. MICRORESONATOR DESIGN

The devices used in this research were fabricated by members of our collaborating group, led by Prof. Minghao Qi. The process begins with the growing of a ~3-μm oxide layer on a silicon wafer to act as a lower cladding. A silicon nitride film of the desired thickness is then applied using low-pressure chemical vapor deposition (LPCVD). Due to high tensile stress between Si_3N_4 and SiO_2, the film is deposited in layers of ~300 nm, with annealing between the steps or trenches etched around the devices to stop cracks propagating from the wafer edge [6] [30].

The bus and resonator waveguides are patterned using electron-beam lithography, featuring the negative-tone resist hydrogen silsesquioxane (HSQ). Unlike photolithography, e-beam lithography does not require a mask. This and its high resolution make it ideal for low-volume production [31]. Finally, a 3-μm oxide upper cladding is applied via LPCVD and high-temperature annealing is performed to remove dangling bonds in the silicon nitride [32]. A cross-section of a fabricated waveguide is shown in Figure 2.1a.

A number of different resonator designs are possible. For high repetition rates (above about 100 GHz), a simple ring is generally most practical (Figure 2.1b). However, larger resonators must adopt some form of folded geometry to fit within the e-beam writing field (Figure 2.1c). Care must be taken to avoid bending radii below approximately 100 μm, as this will lead to excess loss. Other design parameters include the width of the resonator waveguide, which affects the intrinsic loss and dispersion, and the gap between the resonator and bus waveguides, which affects the strength of coupling. Our bus waveguides are standardized at a width of 1 μm, with tapers at either end to improve mode-size and effective-index matching with the input and output fibers [33].

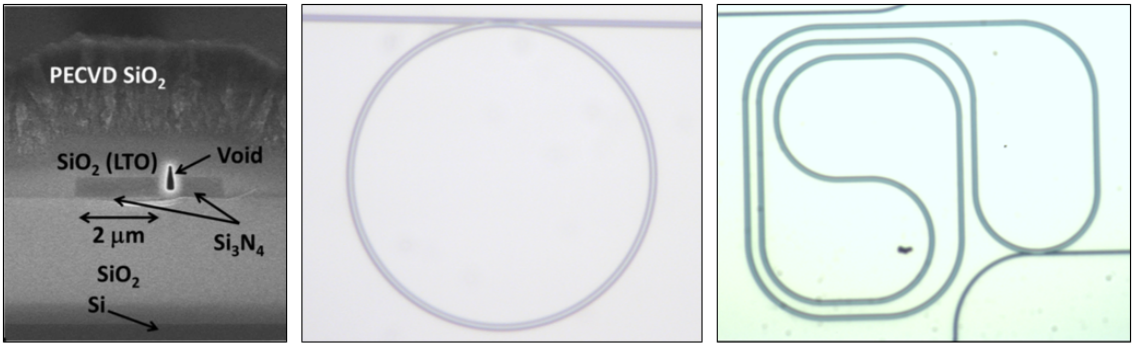

Fig. 2.1. **(a)** Cross-section of resonator (left) and bus (right) waveguides. Sidewalls are nearly vertical, with a tilt angle of 6°. An air gap between the two is often present and may increase coupling loss. Reproduced from [32]. **(b)** Ring resonator with 200 μm radius and 135 GHz FSR. **(c)** 50 GHz resonator. At no point is the bending radius less than 100 μm.

2.1 Q-Factor and Threshold Power

In order for comb generation to initiate, the modulation instability gain for a pair of cavity modes must exceed loss. The maximum round-trip gain, derived from the gain spectrum shown in Figure 1.4b, is $G = 2\gamma P_{res} L$, where L is the circumference of the microring [22]. The round-trip loss is given by [34]:

$$\ell = \frac{n_g L}{c}\left(\frac{1}{\tau_0} + \frac{1}{\tau_{ex}}\right) = \frac{n_g L \omega}{c}\left(\frac{1}{Q_0} + \frac{1}{Q_{ex}}\right) \tag{2.1}$$

where $Q_{ex} = \omega\tau_{ex}$ is the external quality factor, derived from the power coupled to the bus waveguide per round trip, $Q_0 = \omega\tau_0$ is the intrinsic quality factor based on all other sources of loss, and n_g is the group velocity refractive index. Defining the coupling parameter $K = Q_0/Q_{ex}$, the threshold intracavity power for comb generation is therefore:

$$P_{th,res} = \frac{n_g \omega}{2\gamma c Q_0}(1+K) = \frac{n_g A_{eff}}{2 n_2 Q_0}(1+K) \tag{2.2}$$

The intracavity pump power at resonance is related to the power in the bus waveguide according to [34]:

$$P_{res} = \frac{2\lambda_0}{\pi n_g L} \frac{Q_0 K}{(1+K)^2} P_{bus} \tag{2.3}$$

Thus, we find that the threshold input power (after insertion loss) is given by:

$$P_{th,bus} = \frac{\pi n_g^2}{4\lambda_0} \frac{L A_{eff}}{n_2 Q_0^2} \frac{(1+K)^3}{K} \tag{2.4}$$

subsequently referred to only as P_{th}. Several things are important to note. First, the GVD, while it is central to the phase matching condition, does not appear in the threshold power expression. Second, the threshold is lower in smaller rings with tighter mode confinement. The effective group index varies slowly with wavelength but remains close to 2.0, and the nonlinear index is a constant of the material.

The coupling parameter K is also the ratio of the coupling loss to the intrinsic loss. The regions where K is less than one, equal to one, and greater than one are referred to as under-coupled, critically coupled, and over-coupled respectively [35]. Pump power in the ring is maximized at critical coupling, but improving the coupling also increases loss in the sidebands. Therefore, threshold power is minimized with moderate under-coupling, when $K = 0.5$ (Figure 2.2a). The strength of coupling depends on the width of the gap between the resonator and the bus, the dimensions of their waveguides, and the effective length along which coupling occurs. The optimal gap size is smaller for shorter wavelengths; it has been empirically determined to be around 300 nm for a 1 μm pump and a Q_0 on the order of 1 million.

Perhaps the most significant impact on the threshold power, however, comes from the intrinsic quality factor. This depends on several sources of loss, including scattering from material absorption, bending loss, and sidewall roughness. One micron is well away from the major spectral features in the ultraviolet and mid-infrared [18] [21]. However, the material absorption is also also affected by fabrication technique. For instance, annealing removes N-H bonds in the silicon nitride that can act as absorption centers [32]. The prevalence of high power damage at 1.06 μm suggests that

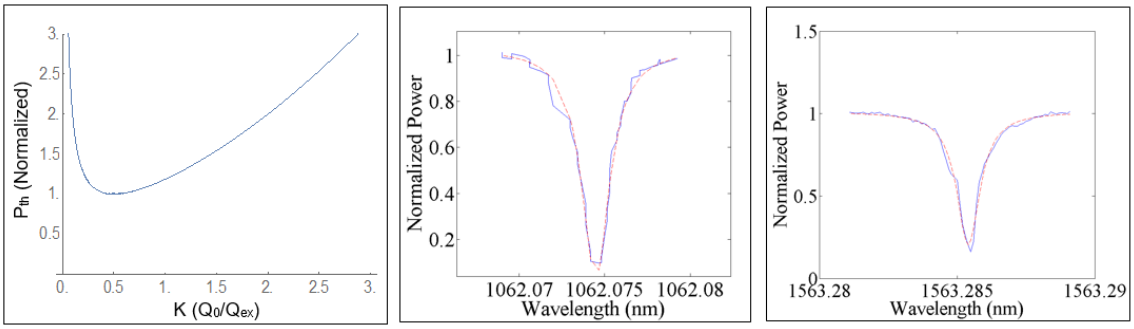

Fig. 2.2. **(a)** Relationship between comb generation threshold and coupling parameter K. Threshold is minimized when moderately under-coupled. **(b)** Fit of resonance in 50 GHz ring. Linewidth of 0.0021 nm, corresponding to loaded quality factor Q_L of 0.5 million. An uncertainty on the order of 10% is expected for both figures. With bus-resonator gap size of 200 nm, ring is expected (but not confirmed) to be over-coupled with $Q_0 = 1.3$ million. **(c)** Fit of C-band resonance on same ring. Stronger over-coupling and linewidth of 0.0010 nm, giving $Q_L = 1.5$ million and $Q_0 = 5.5$ million.

absorption losses should be higher than at 1.55 μm. Bending loss depends on the bending radius and mode shape, but in general decreases with frequency [36].

Scattering loss, on the other hand, increases strongly with frequency. For a typical roughness profile produced by etching during fabrication, scattering from the sidewalls scales as $1/\lambda^4$ [37]. This leads, in general, to lower intrinsic quality factors at 1.06 μm than in the same ring at 1.55 μm. For example, a 50 GHz ring with waveguide dimensions of 300 nm by 3 μm was found to have typical intrinsic quality factors of approximately 1.3 million at 1.06 μm and approximately 5.4 million at 1.55 μm (Figure 2.2b-c). As the top and bottom surfaces of the waveguide are typically much smoother, the scattering loss can be reduced by lowering the film thickness, thus reducing the sidewall area with which the light interacts, or by increasing the waveguide width, thus decreasing the strength of the light's interaction with the sidewalls. A tight bending radius may also increase scattering loss by pushing the mode toward the outer edge of the waveguide [32].

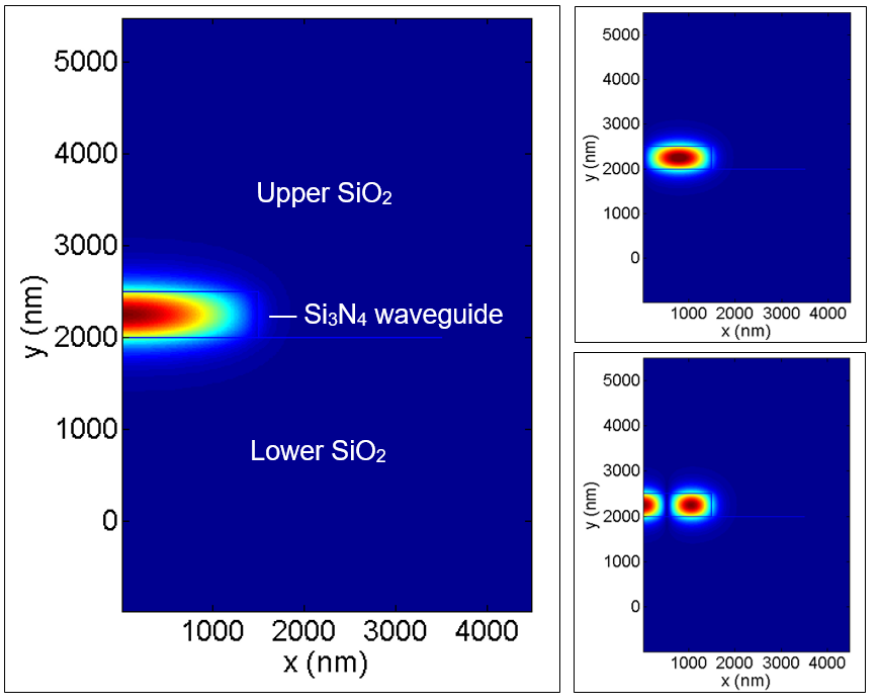

Fig. 2.3. The first three TE modes of a 500x3000 nm waveguide, simulated by WGMODES. They are later identified by their mode numbers as TE1, TE2, and TE3. The field left of the y-axis is assumed to be either symmetric or antisymmetric to the right side. This approximation can be made when the resonator's radius of curvature is much greater than the waveguide width.

2.2 Dispersion Engineering

As noted in the introduction, anomalous group velocity dispersion is a requirement for comb generation to begin. This can be achieved by exploiting local disturbances from mode interactions or by creating a broad anomalous region through careful resonator design, a practice referred to as dispersion engineering. GVD in a waveguide is influenced by both the core and cladding material and the waveguide geometry. The former is readily available from reference sources, but the latter requires numerical simulation of the mode of interest. This was accomplished using the open-source finite difference mode solver WGMODES [38].

This package operates through MATLAB and takes as input a cross-sectional mesh of waveguide and cladding refractive indices and a free-space input wavelength. This is used to compute the electric and magnetic vector fields of the optical eigenmodes, as well as the effective refractive indices for those modes (Figure 2.3). Solving for the same mode number over a range of wavelengths allows us to fit a polynomial to $n_{eff}(\lambda)$. This can give us the effective group index via:

$$n_g = n_{eff} - \lambda \frac{dn_{eff}}{d\lambda} \tag{2.5}$$

which can be used to estimate the FSR of the mode for a given ring radius. The dispersion parameter is given by:

$$D = -\frac{\lambda}{c} \frac{d^2 n_{eff}}{d\lambda^2} \tag{2.6}$$

Waveguide dispersion follows a roughly parabolic profile near its peak. In general, thicker films have more anomalous dispersion. Wider waveguides have their anomalous dispersion peak farther toward the red end of the spectrum, and also have more normal dispersion. However, fabrication of films thicker than 600 nm is more difficult, and generally entails lower Q factors [32]. At a thickness of 800 nm, near the practical limit, a waveguide width below 1700 nm is necessary to acheive anomalous dispersion at $\lambda = 1.06$ μm. At a thickness of 600 nm, the width must shrink to 1200 nm.

In 2012, a group succeeded in engineering rings with anomalous dispersion at 1 μm and using them to generate combs [7]. For a 230 GHz ring with 725x1000 nm waveguides, they reported a loaded quality factor (accounting for both intrinsic and coupling loss) of 250,000 and a comb generation threshold of 40 mW. They did not report their intrinsic quality factor or coupling parameter, but to achieve so low a threshold their ring would have to be strongly over-coupled, with Q_0 on the order of 2 million. If the ring were under-coupled with $K = 0.5$ and $Q_0 = 375,000$, a threshold power of 170 mW would be expected. A comb generated from this ring can be seen in Figure 2.4.

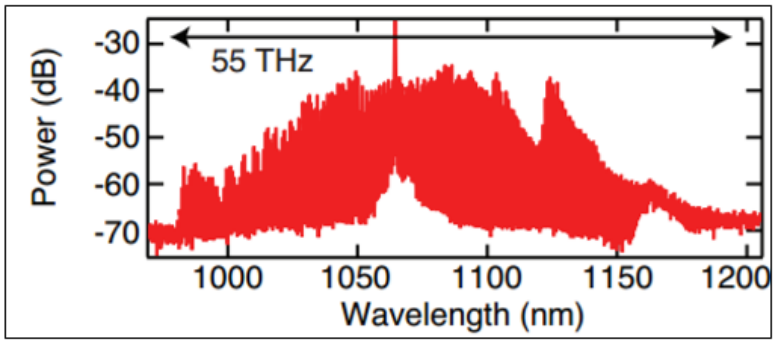

Fig. 2.4. Anomalous dispersion frequency comb reported in [7]. Reported threshold power of 40 mW. This spectrum was recorded at 2 W.

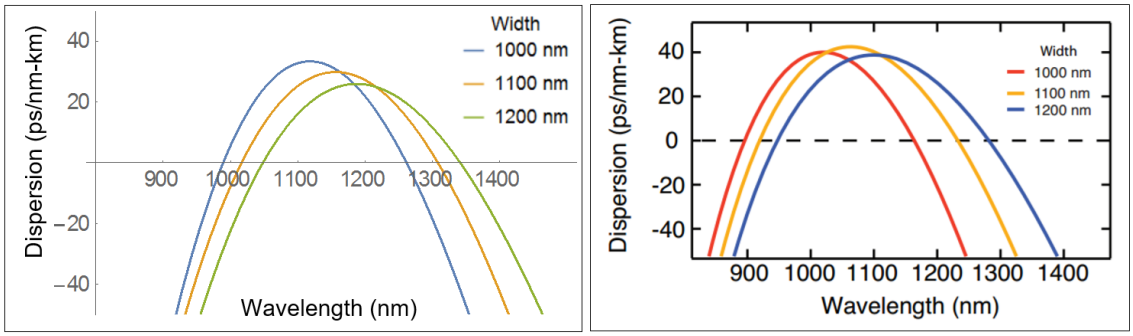

Fig. 2.5. **(a)** Simulated dispersion curves for 600 nm thick waveguides of various widths. **(b)** Curves for the same waveguide dimensions from [7]. Dispersion peaks are higher and farther toward the blue.

They also produced simulations to support their efforts, and while their results are qualitatively similar to mine, they differ somewhat in the position and height of the anomalous dispersion peak (Figure 2.5). There are several possible explanations for this. First, my simulations do not account for slanted sidewalls. Our newer waveguides are nearly rectangular, with sidewall angles of around 6°, due to the thick layer of HSQ used in lithography. However, older techniques produced more trapezoidal cross-sections [32]. Also, my simulations used a newer version of the Sellmeier equation for silicon nitride, developed from mid-infrared observations published in 2015 [21].

Dispersion engineering was evaluated as an avenue for this project, but a set of 1000 nm-wide waveguides fabricated for this purpose showed intrinsic Qs of only 250,000, which would result in threshold powers of around 400 mW. The thicker waveguides needed to achieve anomalous dispersion are also more susceptible to high-power damage (further described in Section 3). Based on these concerns, and because it would be more novel, it was determined that normal-dispersion comb generation using mode coupling would be a more promising area of focus.

Producing strong mode interactions requires another set of design practices. First, the probability of two mode families crossing in the wavelength range of interest should be maximized. This can be accomplished by widening the resonator waveguide, thus increasing the number of transverse modes supported, or by increasing the circumference of the resonator, thus decreasing the FSR of the modes. However, a mode crossing does not guarantee a strong interaction.

Polarization mode coupling in waveguides has been studied in some detail due to the practical applications of an on-chip polarization rotator. Coupling efficiency depends on the asymmetry of the optical field across the x- and y-axes. This can be improved by increasing the sidewall tilt angle and decreasing the waveguide bending radius [39]. Both of these come at the cost of higher radiation loss. A similar principle was found to hold for transverse mode coupling. This was suppressed for narrower waveguide cross-sections, purportedly due to the greater symmetry of the supported modes [40].

2.3 Design Trade-Offs

Having laid out the theory, what is the optimal resonator design for improving the likelihood of mode coupling within the range of our amplifier while maintaining comb generation thresholds that minimize the risk of high power damage? There are several trade-offs to consider here.

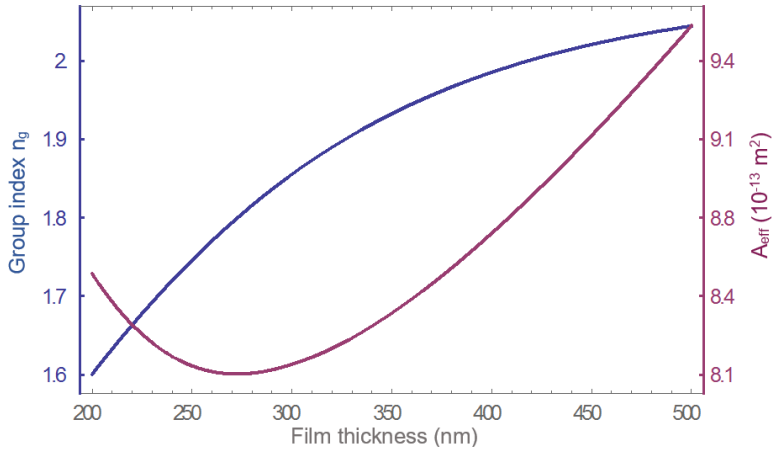

Fig. 2.6. Group index and effective area versus film thickness for a 2.5 μm-wide waveguide. More power is carried in the cladding for very thin films, resulting in a group index closer to the 1.46 of SiO_2. Mode area also begins to grow as containment weakens.

The risk of thermal shock, one of our major high power failure modes, appears to increase for film thicknesses above about 550 nm. If attempting to engineer anomalous dispersion it is necessary to go above this in order to maintain reasonable waveguide widths; otherwise it is better to stay below. Thinner films also offer the advantages of smaller mode areas and lower sidewall scattering, which lowers threshold power. Below 350 nm the confinement begins to suffer, which can be seen in the falling group index and diminishing mode area returns (Figure 2.6). Effective mode area can be calculated from the simulated field cross-section using

$$A_{eff} = \frac{\left(\int I dA\right)^2}{\int I^2 dA} \approx \frac{\left(\sum |E|^2\right)^2}{\sum |E|^4} dA \tag{2.7}$$

Wider waveguides also reduce sidewall scattering, as well as supporting more transverse modes and stronger mode interactions. Simulations indicate that three TE modes should be possible at 1.06 μm for waveguide dimensions of 400x2400 nm versus 400x2900 nm at 1.55 μm. However, these exact numbers have not been confirmed by experiment. These gains come at the price of stronger normal dispersion, particularly when the film thickness is low. This should not be a major problem when simply

attempting to generate a frequency comb. It will, however, limit the bandwidth of generated combs and thus their practical utility. Wider waveguides will also increase the threshold power due to larger mode area.

The other major factor controlling the prevalence of mode interactions is the resonator circumference. However, this scales linearly with the threshold power. The optimal length therefore depends on the quality factor we can expect for a given ring. Assuming ideal coupling, a ring with $Q_0 = 1.0$ million, a cross section of of 400x2500 nm, and a radius of 200 μm will have a threshold power of 90 mW, which should be relatively safe from high power damage. If Q_0 can be raised to 2 million, our 50 GHz resonator format should be easily usable with a threshold of 55 mW. It is important to note that this is only an estimate, and the experimental reality is likely to be more complicated.

3. EXPERIMENTAL METHODS AND RESULTS

Our resonators are fabricated in batches on silicon wafers, then cleaved into chips with 10-20 devices a piece. When a new fabrication arrives, it is first characterized with a low-power transmission scan. This can be used to determine intrinsic Q factor, coupling strength, the presence of mode interactions, etc. If the results of this are promising, the channel is then tested for comb generation at high power.

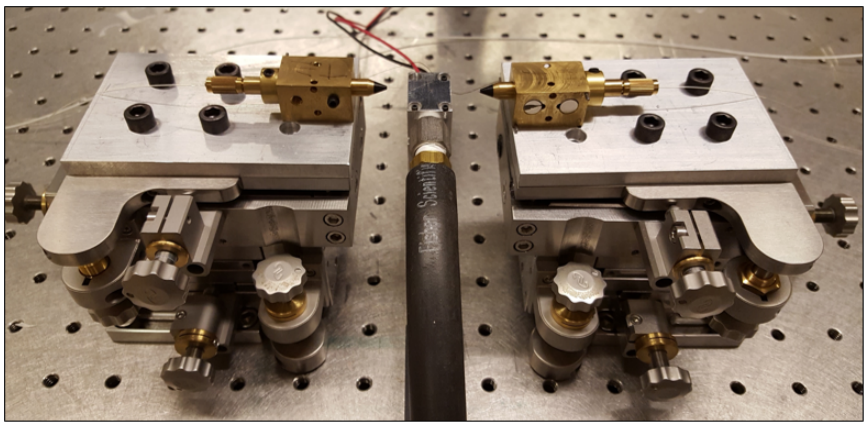

Fig. 3.1. Sample stage used in all experiments. Capable of 3D translation, pitch, and yaw. Custom PM fiber holders at top can be used to deterministically set polarization.

Both types of experiment are done using the stage in Figure 3.1. A vacuum pump is used to stabilize the chip in the center, and the 5-axis translation/rotation stages on either size line up lensed fibers to couple light into and out of the bus waveguide (or drop waveguide, where appropriate). They are aided by U-grooves etched into the sides of most of our chips, which help stabilize the fibers under high power. Coupling efficiency depends on these fibers being placed with micron-scale accuracy, so a video

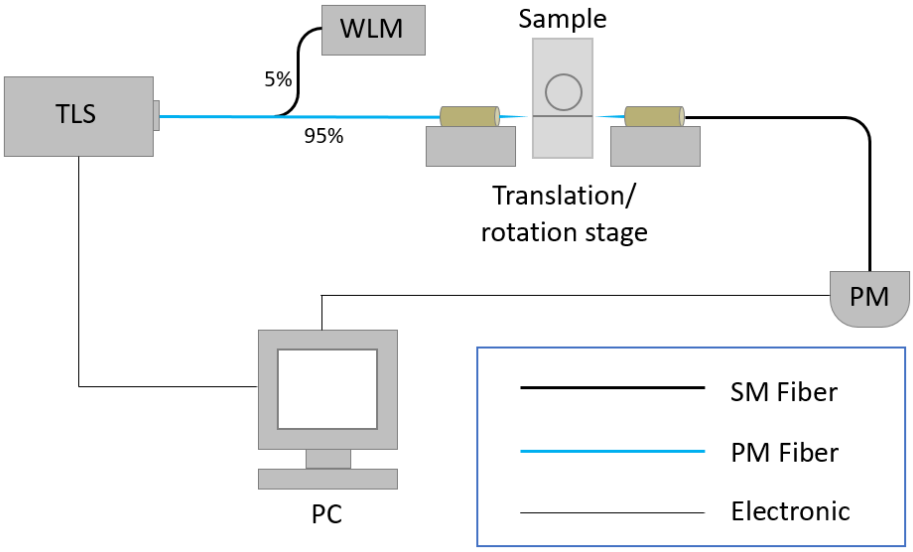

Fig. 3.2. Transmission scan setup. TLS: Tunable laser source, WLM: Wavelength meter, PM: Power meter.

microscope is used to aid in alignment. At optimal coupling, insertion loss is generally on the order of 2.5 dB per facet.

Unlike our setups for use at 1.55 μm, the 1.06-μm version uses polarization-maintaining (PM) fiber. The holders for the lensed input and output fibers can be rotated to set the polarization and then locked in place, eliminating any uncertainly about whether the TE or TM mode is being excited. Initial setting of the polarization is done by eye using a collimating lense, a birefringent crystal, and an IR card, so uncertainty on the order of 10° is to be expected.

3.1 Low Power Characterization

The setup for performing a low-power transmission scan is shown in Figure 3.2. A New Focus TLB-6721 tunable diode laser is used as the source. It has a wavelength range of 1030 to 1070 nm with a resolution of 0.01 nm, can scan at speeds ranging from 0.01 nm/s to 10 nm/s, and has a maximum output power of 19 mW, though typically only about 3 mW is used during transmission scans to prevent thermal

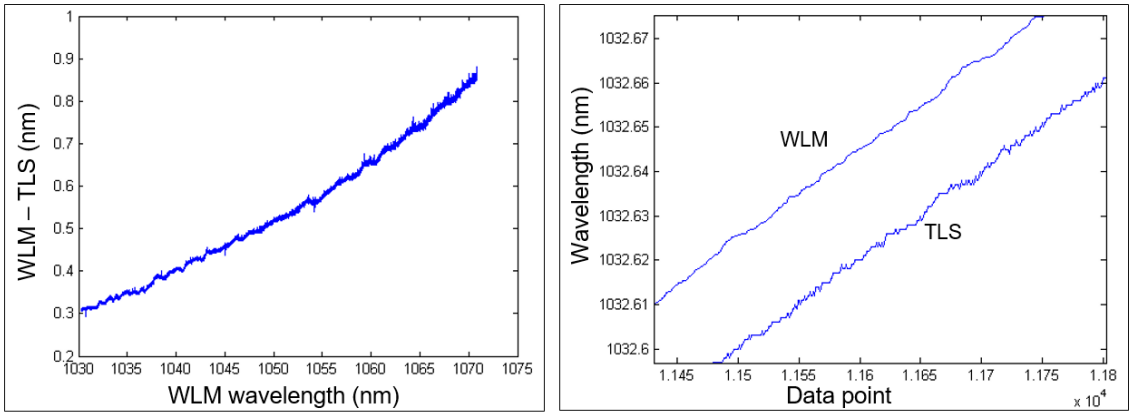

Fig. 3.3. **(a)** Deviation of TLS wavelength self-reporting from WLM measurements. This data was used to fit a calibration curve for easier tuning. **(b)** Comparison of WLM and TLS wavelength data during a scan. Note that the WLM curve is not completely smooth. This is most likely due to variations in scan speed and measurement timing jitter.

resonance shifts. A fiber coupler sends 5% of the output power to a HighFinesse WS/6-200 wavelength meter with an uncertainty of ±200 MHz (≈ 0.001 nm) and a measurement frequency of up to 300 Hz (limited by the integration time).

The other 95% is sent to the sample stage. The output from the sample goes to a Thorlabs power meter, of which we have several in the lab. The most commonly used was the S145C, which contains an integrating sphere and an InGaAs detector. It has a 5% uncertainty and an operating range of 1 μW to 3 W (-30 to +35 dBm), and is driven by a PM100A power meter console with a bandwidth of up to 100 kHz.

To begin the scan, the tunable laser source (TLS) is ordered to scan continuously over the desired range at the minimum speed of 0.01 nm/s. The wavelength meter (WLM) and power meter (PM) are then queried at specified intervals until the scan is due to complete. In the first iteration of the setup, wavelength data was obtained using the laser's built-in query function. However, this was found to be poorly calibrated and imprecise (Figure 3.3).

Given the fixed speed of the laser, the only way to increase resolution is by maximizing the query rate of the WLM and PM. For a laser power of 3 mW, a WLM integration time of 10 ms was generally used. The software used to retrieve the measurement introduced some delay as well, so a sampling period of 20 ms was settled on to avoid repeated points. The power meter, on the other hand, can be sampled as quickly as the MATLAB loop allows, which in practice is three times the rate of the WLM. The rate of wavelength scanning is assumed to be roughly constant between WLM reads. This gives us a scan resolution of 6.67×10^{-5} nm, or on the order of 20 points per resonance.

3.1.1 Quality Factor Fitting

One of the most important functions of transmission scans is the determination of the intrinsic Q factor for a resonator. The through-port transmission near an isolated resonance is given by [41]:

$$T = \frac{(\lambda - \lambda_0)^2 + (FSR_\lambda/4\pi)^2\left(\kappa_p^2 - \kappa_e^2\right)^2}{(\lambda - \lambda_0)^2 + (FSR_\lambda/4\pi)^2\left(\kappa_p^2 + \kappa_e^2\right)^2} \tag{3.1}$$

where λ_0 is the center wavelength of the resonance, $FSR_\lambda = \lambda^2/ct_R$ is the wavelength distance between resonances, κ_p^2 is the fractional intrinsic power loss per round trip, and κ_e^2 is the fractional coupling power loss per round trip. The loaded quality factor, which accounts for loss from both coupling and intrinsic sources, is defined as:

$$Q_L = \omega_0\tau = \frac{2\pi c}{\lambda_0}\frac{t_R}{\kappa_p^2 + \kappa_e^2} = \frac{2\pi\lambda_0}{FSR_\lambda(\kappa_p^2 + \kappa_e^2)} \tag{3.2}$$

Therefore, the loaded quality factor for a given resonance can be found by fitting the Lorentzian function

$$P(\lambda) = a\frac{(\lambda - \lambda_0)^2 + b}{(\lambda - \lambda_0)^2 + c} \tag{3.3}$$

to the transmission data and evaluating $Q_L = \lambda_0/2\sqrt{c}$. When the linewidth $\Delta\lambda \ll \lambda_0$, as is the case in any high-Q optical resonator, this is equivalent to $Q_L = \lambda_0/\Delta\lambda$.

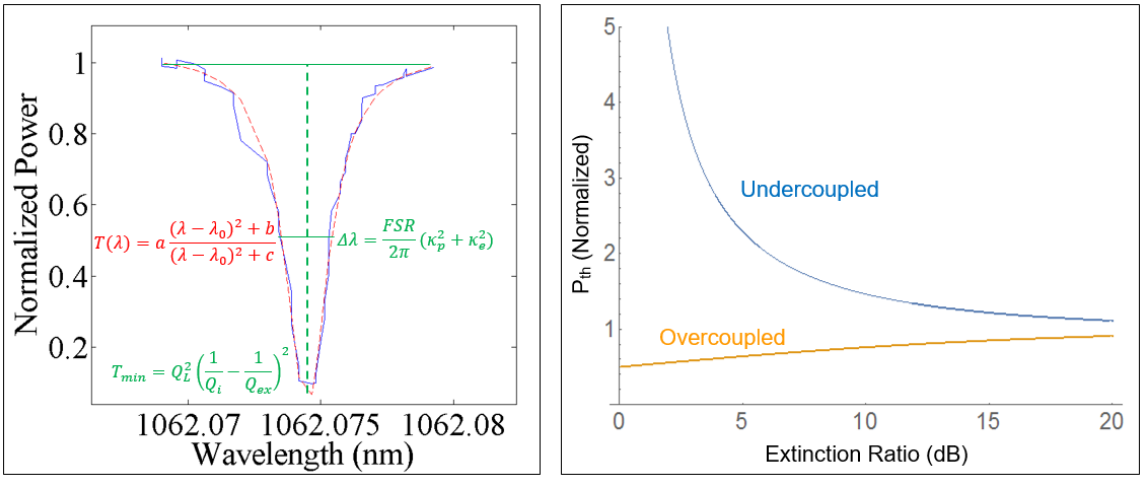

Fig. 3.4. **(a)** Fit of resonance with $Q_L = 0.5$ million. If over-coupled, $Q_0 = 1.3$ million, and if under-coupled, $Q_0 = 0.9$ million. **(b)** Threshold power versus extinction ratio with Q_L held constant.

To obtain Q_0, we must separate coupling losses from intrinsic losses. This is most easily done by looking at the extinction ratio, or the ratio between the power transmitted far from resonance and the minimum power when tuned perfectly into resonance. This is equivalent to the inverse of the transmission function in Equation 3.1. Setting λ equal to λ_0:

$$T_{min} = \frac{(FSR_\lambda/4\pi)^2\left(\kappa_p^2-\kappa_e^2\right)^2}{(FSR_\lambda/4\pi)^2\left(\kappa_p^2+\kappa_e^2\right)^2} = \frac{(\lambda_0/2Q_0-\lambda_0/2Q_{ex})^2}{\lambda_0^2/4Q_L^2} = Q_L^2\left(\frac{1}{Q_0}-\frac{1}{Q_{ex}}\right)^2 \quad (3.4)$$

Using the relationship $1/Q_L = 1/Q_0 + 1/Q_{ex}$, we can eliminate the external quality factor and find that

$$T_{min} = \left(\frac{2Q_L}{Q_i}-1\right)^2 \quad (3.5)$$

$$Q_0 = \frac{2Q_L}{1\pm\sqrt{T_{min}}} \quad (3.6)$$

In terms of our Lorentzian fitting function, this is $Q_0 = \lambda_0/(\sqrt{c} \pm \sqrt{b})$. The sign in the denominator depends on whether κ_p^2 or κ_e^2 is larger, *i.e.* whether the resonator is under- or over-coupled. T_{min} will fall to zero at critical coupling, and increase as one moves in either direction. The coupling parameter is given by

$$K = \frac{2Q_L}{1 \pm \sqrt{T_{min}}} \cdot \frac{1 \mp \sqrt{T_{min}}}{2Q_L} = \frac{1 \mp \sqrt{T_{min}}}{1 \pm \sqrt{T_{min}}} \tag{3.7}$$

Substituting 3.6 and 3.7 into the threshold power equation, we find that

$$P_{th} \propto \frac{(1+K)^3}{Q_0^2 K} = \frac{2}{Q_L^2(1 \mp \sqrt{T_{min}})} \tag{3.8}$$

This means that two identical-looking resonances can have radically different comb generation thresholds, especially if extinction ratios are low (Figure 3.4). Resonators with large gaps sizes can generally be assumed to be under-coupled, but otherwise the coupling regime can be difficult to determine at first glance. It can be measured directly by examining the phase response of the resonator as described in [42], though this has not yet been implemented at 1 micron. More examples of transmission scans and their resulting Qs can be seen in Appendix A.

3.1.2 Dispersion and Mode Coupling

The different "families" of transverse modes in a microresonator are easily distinguishable in transmission scans, as they have different Q factors, coupling strengths, and free spectral ranges (Figure 3.5). The latter presents the easiest means of identifying them. As suggested in [32], finite difference simulation can be used to find the group index for a given mode number, and this can be used to calculate its free spectral range via $FSR = c/Ln_g$. It should be noted that the transmission spectrum will not necessarily display all the modes which can in theory be supported by a given waveguide. The higher-order modes may have high loss or poor coupling with the bus waveguide [43].

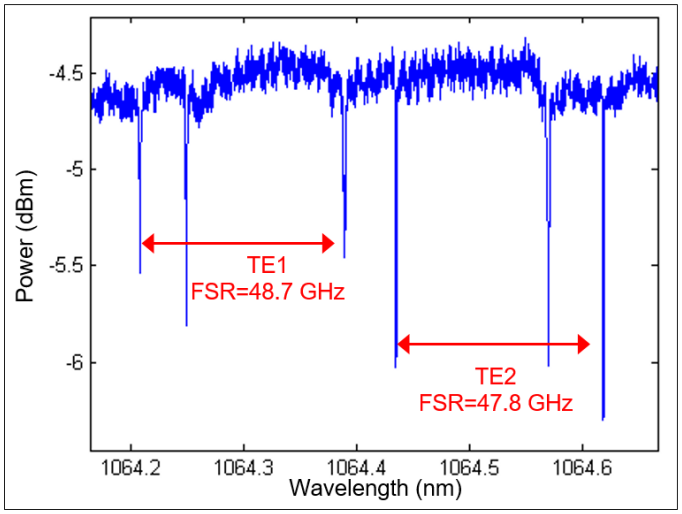

Fig. 3.5. Transmission scan of 600x2000 nm ring with two transverse electric (TE) mode families. TE1 has an FSR of 48.7 GHz compared to a simulated value of 48.5 GHz. TE2 has a measured FSR of 47.8 GHz compared to a simulated 47.2 GHz.

Because FSR depends on group index, it can also be used to measure dispersion [35]. Using Equations 1.1 and 1.2, the relative phase shift applied to two frequencies ω and ω_0 as they travel the length of a resonator is:

$$\phi(\omega) - \phi(\omega_0) = -[\beta(\omega) - \beta(\omega_0)]L = -\Big[\beta_1(\omega - \omega_0) + \frac{\beta_2}{2}(\omega - \omega_0)^2\Big]L \tag{3.9}$$

Differentiating with respect to ω yields:

$$\frac{\partial\phi}{\partial\omega} = -\big[\beta_1 + \beta_2(\omega - \omega_0)\big]L \tag{3.10}$$

Resonant modes must by definition fit an integer number of wavelengths within the cavity, so the relative phase shift for frequencies spaced one FSR apart is 2π. Because the free spectral range is much smaller than the resonant frequency, we can write:

$$\frac{\partial\phi}{\partial\omega} = \frac{2\pi}{2\pi FSR} \tag{3.11}$$

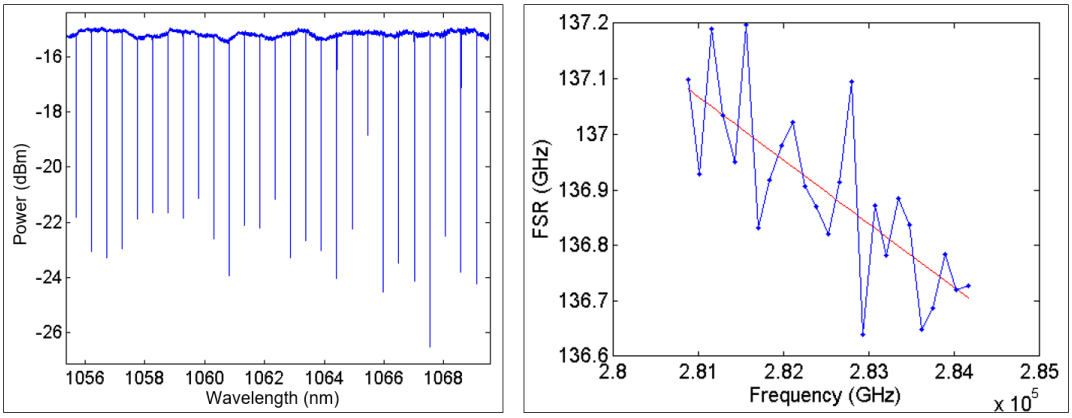

Fig. 3.6. Dispersion measurement for a resonator of radius 200 μm and cross section 300x1300 nm. The measured result was -850 ps/nm-km, compared to a simulated value of -685 ps/nm-km. At this width, only one mode is expected to be supported.

$$FSR(\omega) = -\frac{1}{L}\frac{1}{\beta_1 + \beta_2(\omega - \omega_0)} = -\frac{1}{\beta_1 L}\left[1 + \frac{\beta_2}{\beta_1}(\omega - \omega_0)\right]^{-1} \tag{3.12}$$

Applying the binomial approximation, we find that

$$FSR(f) = -\frac{1}{\beta_1 L} + \frac{2\pi\beta_2}{\beta_1^2 L}(f - f_0) \tag{3.13}$$

Experimentally, this means that the linear function $FSR(f - f_0) = a_0 + a_1(f - f_0)$ can be fit to a plot of free spectral range versus frequency, and β_2 can be calculated via

$$\beta_2 = -\frac{a_1}{2\pi L a_0^2} \tag{3.14}$$

An example of this method can be seen in Figure 3.6. The fundamental TE mode of a waveguide with dimensions of 300x1000 nm is shown to have a dispersion of -850 ps/nm-km, compared to a simulated value of -685 ps/nm-km. However, this comes with significant uncertainty due to the large variation of the data points around the trend line. This is likely caused by resonance shifts due to temperature fluctuations over the course of the scan. A standard transmission scan over 15 nm using the

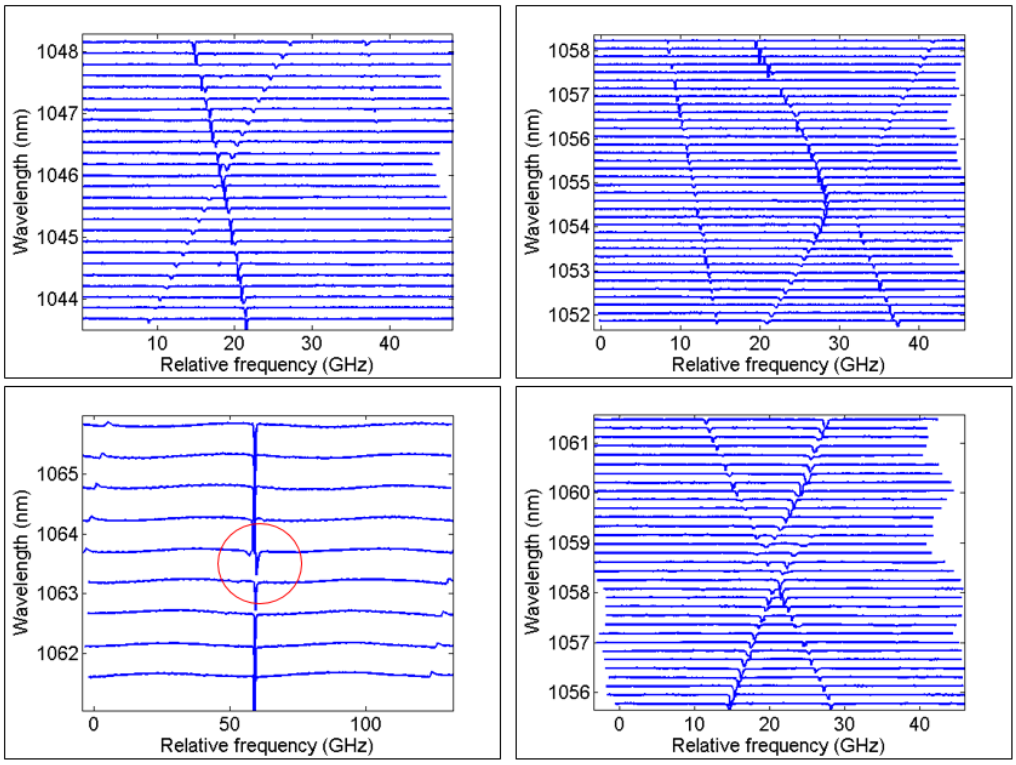

Fig. 3.7. **(a)** Mode crossing without coupling in 50 GHz resonator. Note the visible left-concavity, indicating strong normal dispersion. **(b)** Strong mode interaction in same resonator, creating a narrow region of ≈800 ps/nm-km normal dispersion. **(c)** Weak mode interaction in 137 GHz resonator, but still sufficient to flip sign of dispersion on one resonance. **(d)** Interaction with mode not visible in TE transmission scan of 50 GHz resonator. Either a TM or poorly-coupled higher-order TE mode.

wavelength meter takes 25 minutes. The best way to address this problem is by speeding up the scan rate as described in [35], using RF beat notes from an external frequency comb to establish resonance positions. Barring the construction of such a setup, the only options are to obtain better statistics by extending the range of the sweep or averaging over multiple scans.

Mode coupling can also be detected using transmission scan data. This is done by slicing the scan into one-FSR segments and stacking them vertically such that the resonance dips from one mode family line up. If an interaction exists, it will perturb

the FSR in a manner similar to the simulation in Figure 1.5. Mode coupling has been detected in several devices.As seen in Figure 3.7, the interaction does not need to be very strong to change the sign of the GVD. The local dispersion can be quantified by finding the asymmetry factor $D_m = \omega_m - \omega_0 - (\omega_0 - \omega_{-m})$ and applying Equation 1.12:

$$D_{eff} = \frac{n_{eff} D_m}{2\pi m^2 \lambda^2 \mathrm{FSR}^2} \tag{3.15}$$

Because calculations derived from only three resonances are bound to be imprecise, the sign of the dispersion can be also identified by inspection by noting the concavity of the mode plot. Concave-right corresponds to FSRs growing with frequency, and thus anomalous dispersion. Coupling can also take place with modes that are not visible in the transmission spectrum, such a higher-order mode with poor coupling or the opposite polarization (Figure 3.7d). When the coupling region on a device overlaps with the effective range of the fiber amplifier, it becomes a good candidate for high-power testing.

3.2 High Power Characterization

As the maximum output of the tunable laser system is 19 mW, more power is needed to attempt comb generation. This is accomplished using a Keopsys CYFA-PB ytterbium-doped fiber amplifier (YDFA). It has a stated wavelength range of 1060 to 1090 nm and a maximum output power of 33 dBm (2 W). The output passes through an Ascentta polarization-maintaining isolator with an insertion loss of 0.7 dB to prevent instability due to back-reflection. After the sample stage, 95% of the light is sent to a power meter, which aids in maintaining good coupling between the lensed fibers and the chip, and 5% is sent to an optical spectrum analyzer (OSA), passing through a variable attenuator on the way. A diagram of the high-power setup is shown in Figure 3.8.

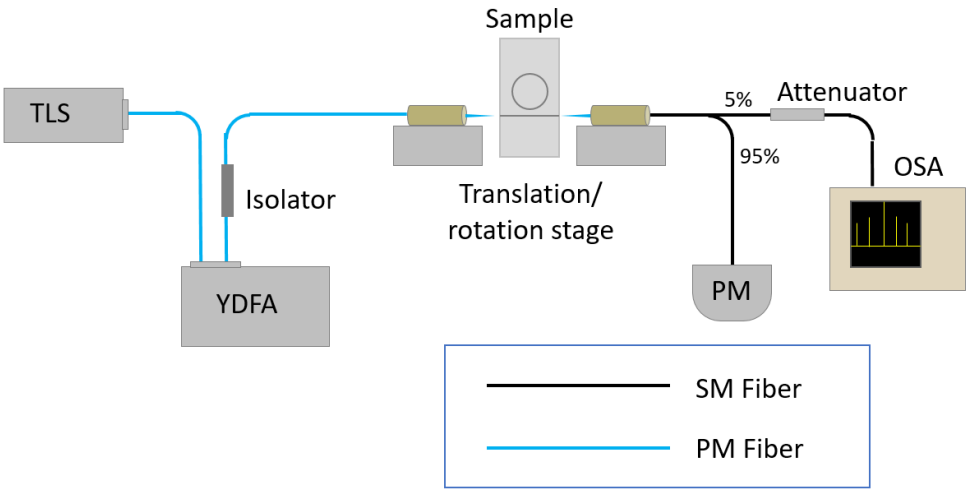

Fig. 3.8. Setup for attempting comb generation at high power. YDFA: Ytterbium-doped fiber amplifier, OSA: Optical spectrum analyzer.

The simplest procedure for comb generation is simply to tune carefully into a resonance of interest and watch the OSA for comb lines, increasing power as needed. Tuning must begin from the blue side, as the increasing temperature in the ring will push the resonance toward the red. At some point the pump will overtake the center wavelength and the resonance will jump back to its original position (Figure 3.9). It should be noted that different mode families may experience different thermal shifts, changing the positions of mode crossings under high power [26].

I have encountered several obstacles in working at high power. First, the overlap between the nominal ranges of my tunable laser and amplifier is only 10 nm. The latter supplies sufficient output power down to 1055 nm, but this still leaves only a 15 nm window in which mode interactions can be exploited. This underscores the importance of intelligent device design as described in Section 2, in order to maximize the probability of finding an interaction within this range. Another major issue is the high rate of optical waveguide damage at 1 micron.

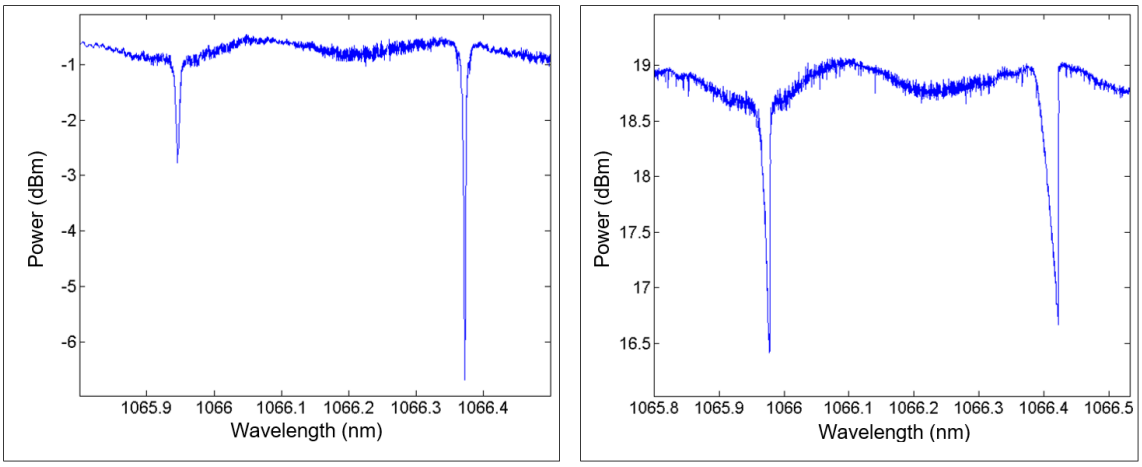

Fig. 3.9. Comparison of low power and high power transmission scans. In the latter case the resonances are asymmetric and shifted to the right.

3.2.1 High Power Damage

The waveguide damage observed thus far can be grouped into two failure modes, both of which render the channel unusable. In the first, a long section of the bus waveguide becomes darkened and opaque. As this damage typically extends all the way back to the input facet, it is likely a case of the fiber fuse effect. This phenomenon has been well-documented in silica fibers, due to the threat it poses to long-haul communications infrastructure [44]. It has also been observed in planar waveguides [45].

The fiber fuse occurs when a section of waveguide is heated to the point where its absorption coefficient begins to increase. Heating then continues in a feedback loop until the core material breaks down, at which point the damage propagates backwards along the waveguide. The section past the initial damage point is unharmed. This initial point can be an imperfection or contamination on the upper cladding (Figure 3.10a) or simply a transition in the waveguide structure (Figure 3.10b). In some cases, the input taper is blown away when the wave reaches the chip edge (Figure

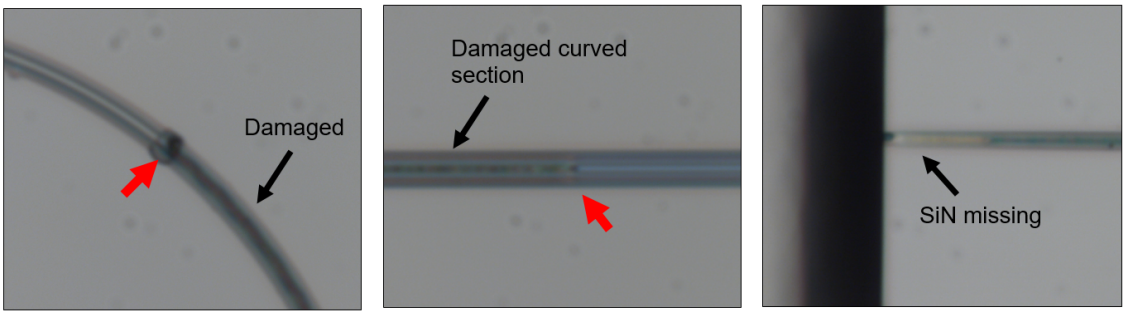

Fig. 3.10. **(a)** Fiber fuse in a 300 nm chip due to dirt or fabrication defect. Initial point marked with red arrow. **(b)** Fiber fuse beginning between straight and curved sections of bus waveguide. **(c)** Input taper destroyed by fiber fuse, without damaging oxide cladding.

3.10c). This type of damage occurs more frequently in thin films due to their smaller mode areas, and thus higher intensities.

The other, more spectacular, failure mode occurs when the input end of the bus waveguide suddenly disintegrates, leaving a hollow in the surrounding oxide several tens of microns wide (Figure 3.11). Frequently, the tip of the lensed input fiber is damaged as well. Initially, it was theorized that this may be due to strong absorption by the substrate, as silicon has a bandgap corresponding to $\lambda = 1100$ nm. However, some waveguides can be safely operated up to the maximum 2 W amplifier output, whereas others have failed under as little as 150 mW of power. In addition, simply focusing high power onto a blank section of the chip did not reproduce the effect.

Indeed, SEM images of the damaged waveguides have shown that the hollow does not extend beyond the lower SiO_2 cladding, failing to penetrate into the silicon substrate (Figure 3.11c-d). Our current working theory is that heating of the chip edge increases the tensile stress between the silicon nitride and silicon dioxide to the point where it eventually shatters. As such, this type of damage is more common in chips with thicker films, whose fabrication creates higher intrinsic stress [30]. The heating required to produce this damage could come from several different sources, including dust in the coupling area, imperfections in the fabrication, and occasionally

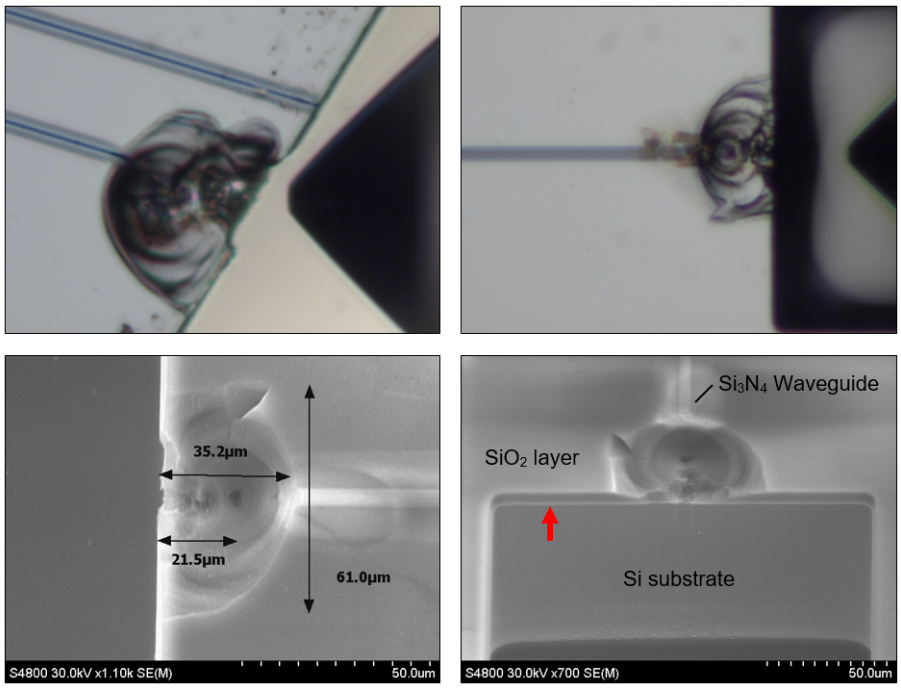

Fig. 3.11. **(a)** Thermal stress failure in a 770 nm chip. Lensed fiber was damaged and had to be replaced. **(b)** Failure in 580 nm chip, initiated by fiber fuse. **(c)** SEM top view of damage in (b), showing dimensions of hollow. **(d)** SEM oblique view. Boundary between silicon substrate and oxide layer is marked by red arrow.

a fiber fuse. Heating of the silicon substrate, even if if does not itself display damage, could also play a role.

It is difficult to precisely estimate the threshold for high power damage, as it varies from channel to channel and is generally something we wish to avoid. However, one is generally safe if they stay below approximately 200 mW. Assuming insertion loss of 2.5 dB per facet, this means chip design should focus on achieving comb generation threshold powers below 115 mW. Risk can also be minimized by keeping film thickness between 400 and 550 nm, beyond which the incidence of damage appears to increase. Finally, methods can be developed for the easier detection of comb generation, requiring less time and power than the OSA.

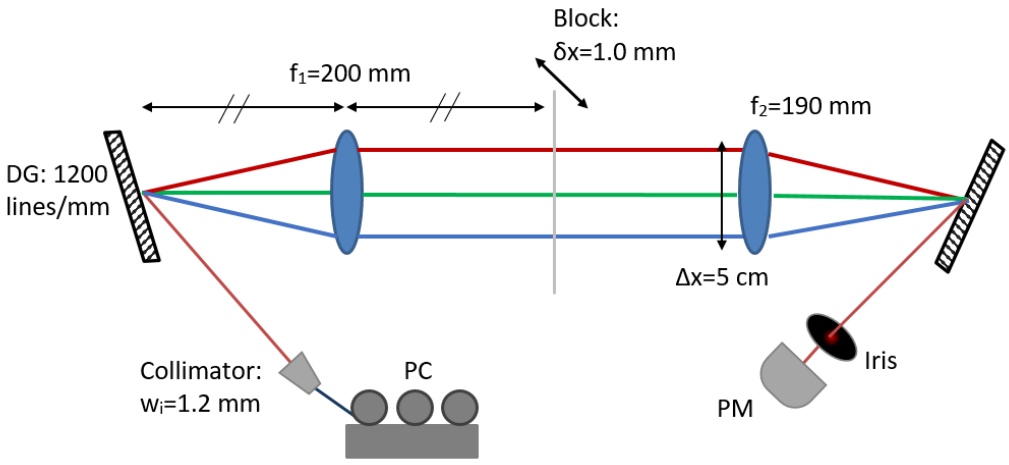

Fig. 3.12. Diagram of pump blocker. Light from sample stage enters the setup through a polarization controller (PC). Both diffraction gratings (DG) are identical. Ideally f_1 would equal f_2, but a slight difference is acceptable. A thin black wire at the focal plane of the lenses can be moved to block different spectral components. An iris before the power meter blocks stray light from reflections and lens aberration.

3.2.2 Pump line blocking

One means of comb detection commonly employed at 1550 nm is using a pulse shaper to block the pump wavelength as it sweeps through resonance. The comb lines are not attenuated, so they are easily detectable as excess power. In lieu of purchasing a commercial pulse shaper, a free-space version can be constructed from basic optical components. A diagram of the resulting setup can be seen in Figure 3.12.

Light from a collimator strikes a diffraction grating, and its angularly dispersed components are focused by the first lens into spatially dispersed spots along the lens's focal plane. In essence, the grating and lens perform a frequency-to-space Fourier transform on the input beam [46]. The frequency components of the light can be individually manipulated by a mask in the focal plane. In commercial models, this takes the form of a programmable spatial light modulator, but to block the pump beam a thin black rod on a translation stage will serve just as well.

In the first iteration of this setup, a free-space power meter was placed immediately after the block, but this was found to provide insufficient rejection of stray pump light. This opened up two options: another grating-lens pair could be used to reassemble the beam, or a plane mirror could direct the light back through the first half of the setup. The latter structure would save on space and alignment time, but its resolution would be limited by the inability to place the block exactly at the focal plane, and it would also require the purchase of a fiber circulator [47]. In light of this, a transmission geometry was adopted.

Because the block can be moved at will, the spectral range of the shaper is determined by the aperture of the input lens, in this case 5 cm. Not all of this is usable due to aberration, but it can provide a first-order estimate of the number of comb lines collected. The lens is placed one focal length or 20 cm away from the grating, and the angle of incidence is controlled by the grating equation:

$$d(\sin\theta_i + \sin\theta_d) = m\lambda \tag{3.16}$$

The grating used has $d = 0.001/1200 = 0.83\ \mu$m, and the angle with the collimator is set to $\theta_i = 65^\circ$. The order of diffraction m is assumed to be 1. This allows us to solve for the diffraction angle:

$$\theta_d = \arcsin\left(\frac{m\lambda}{d} - \sin\theta_i\right) \tag{3.17}$$

If we make the conservative estimate that half of the lens diameter is aberration-free, an angular variance of $\Delta\theta_d = \arctan(2.5/20) = 7^\circ$ is allowed. Assuming a center wavelength of 1060 nm, this gives us a spectral range of $\Delta\lambda = 100$ nm, or 27 THz. This will accommodate over 100 comb lines from a radius-100 μm microring. Good transmission has been confirmed over the 40-nm bandwidth of my tunable laser. The range attenuated by the block is given by

$$\delta\lambda = \delta x \frac{d\cos\theta_d}{f} \tag{3.18}$$

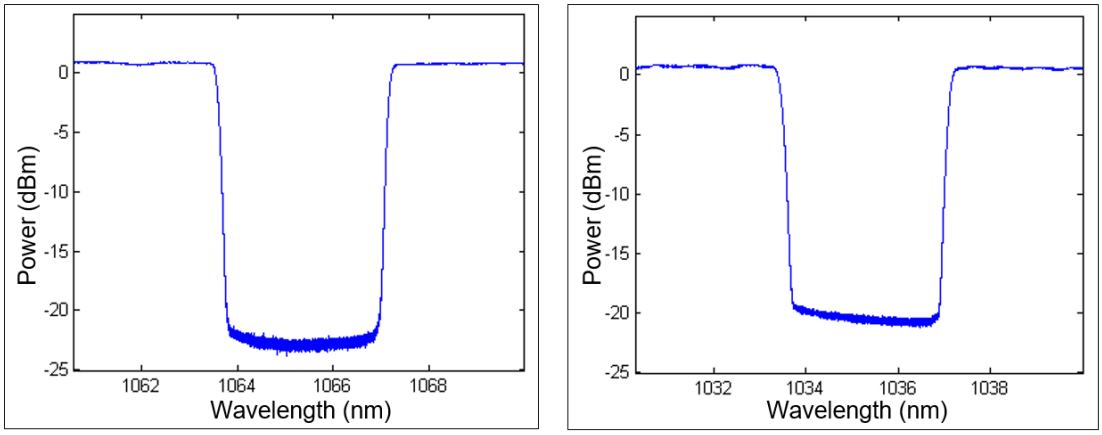

Fig. 3.13. **(a)** Transmission of pulse shaper with the block centered at 1065 nm. Bandwidth of 3.55 nm and extinction ratio of 24 dB. **(b)** Transmission with the block at 1035 nm, showing a bandwidth of 3.65 nm. Attenuation lowered to 21 dB, plus greater asymmetry. Both likely due to aberration farther from the centers of the lenses. If the gratings are aligned so that 1062.5 nm light passes through the center of the lenses, this effect should not be significant over the 15 nm range of interest.

where $\delta x = 1.0$ mm is the width of the block. This expression predicts attenuation bandwidths of approximately 3.9 nm within the range of the laser. This agrees fairly well with the experimental value of 3.55 nm obtained at a center wavelength of 1065 nm, corresponding to 950 GHz or four resonances of a 100 μm ring (Figure 3.13a). The discrepancy between predicted and experimental values is likely due to error in the measurement of the setup dimensions and the finite spot size of the laser at the focal plane. This spot size is predicted to be [46]

$$w_0 = \frac{\cos\theta_i}{\cos\theta_d}\frac{f\lambda}{\pi w_i} = 25\ \mu\text{m} \tag{3.19}$$

where $w_i = 1.2$ mm is the beam radius at the collimator. The shape of the falling edge is given by the error function

$$T(\lambda) = \frac{1}{4}\left[1 - \text{erf}\frac{\sqrt{2}(\lambda - \lambda_0)}{w_0\ d\lambda/dx}\right]^2 \tag{3.20}$$

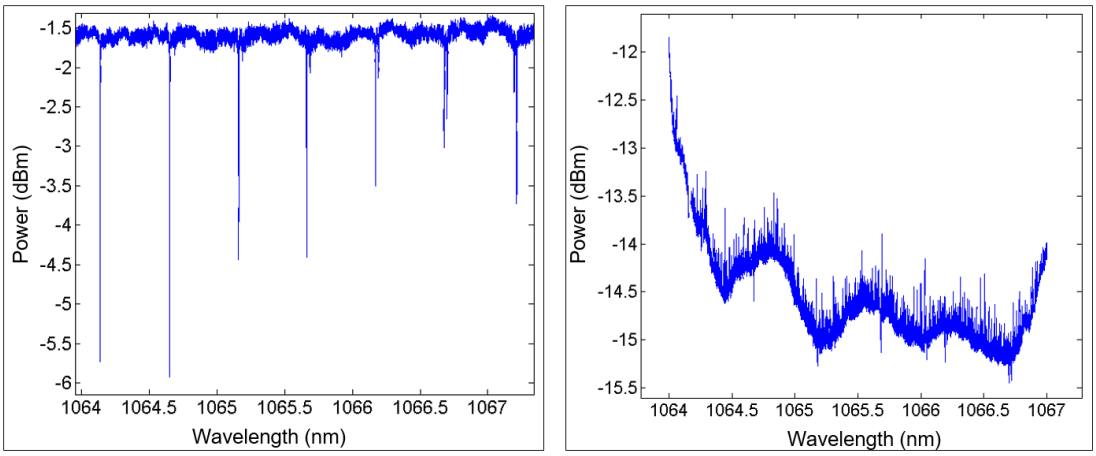

Fig. 3.14. **(a)** Low-power transmission scan of a 130 GHz resonator, showing a polarization mode interaction centered at 1066.5 nm. **(b)** High-power transmission near the mode interaction, with pump line attenuated. Scan taken at pump power of approximately 125 mW. Channel failed at 200 mW.

where λ_0 is the wavelength corresponding to the edge of the block [48]. This is derived from the convolution of a Gaussian beam profile with the step function of the block. Equation 3.16 can be used to find the space-to-wavelength conversion factor $d\lambda/dx = d/f \cos\theta_d = 3.86 \times 10^{-6}$. The error function predicts a spectral distance of 0.053 nm from 75% to 25% transmission. In experiment, this is measured as 0.08 nm, suggesting a larger-than-expected spot size. This may be due to the beam size at the collimator being smaller than the rated value or the block being slighly out of the focal plane.

A maximum of 24 dB attenuation has been achieved using this setup, which should make combs of moderate efficiency easily detectable. However, the attenuation decreases somewhat as one moves toward the edges of the spectral range, likely due to lens aberration (Figure 3.13b). For comparison, the Finisar pulse shaper commonly used in our lab at 1.5 μm is capable of 40 dB of attenuation. The loss for un-attenuated light from the input to the detector is 5 dB.

The pump blocker has not yet seen extensive use, but an example of its transmission in practice can be seen in Figure 3.14. A resonator was probed under high power near a mode interaction, but no comb generation was detected before the channel failed. Nonetheless, this setup could be valuable for future comb detection efforts. Its utility could be further increased by improving its pump attenuation, which could be most easily done by reducing the spot size of light in the blocking plane and improving the rejection of stray light from the room and the pump laser. Methods for achieving the latter include constructing shielding to keep out room light and placing a lens in front of the iris to focus the desired light to a point.

4. SUMMARY

Silicon nitride microresonators represent a promising platform for the generation of optical frequency combs, given their small footprint, CMOS compatibility, and large optical nonlinearity. However, the modulation instability and four-wave mixing processes involved in comb generation have strict phase-matching and quality-factor requirements that can make them difficult to achieve at short wavelengths. This thesis focused on the theory of frequency comb generation, design parameters that affect resonator performance at 1.06 μm, and experimental techniques for characterizing resonators and low and high power.

After investigating dispersion engineering using waveguide mode simulations, it was determined to focus on mode coupling as a route to comb generation. This helped to constrain the parameter space for resonator designs. Waveguide height is limited on the low end by optical confinement and on the high end by high power damage. Wider waveguides can support more modes and higher Q factors, though at the cost of more normal dispersion. Resonator length is a trade-off between mode coupling likelihood and comb generation threshold power.

Methods for experimentally measuring Q factor and dispersion were adapted for use at 1.06 μm, and evidence of transverse mode coupling in this regime was found. The causes of frequent high-power waveguide damage were identified as thermally-induced tensile strain and the fiber fuse effect. Finally, a setup for more easily probing resonators for comb generation was demonstrated.

4.1 Next Steps

Although comb generation at 1.06 μm has thus far proved elusive, the path toward achieving it has been illuminated. First and foremost, more chips should be tested

now that resonator design for this wavelength band has been optimized somewhat. This will increase the likelihood of finding resonators with low threshold powers and properly located mode interactions, and help determine if more design iteration is needed.

The other major priority is to mitigate the effects of high power damage. In the case of the fiber fuse effect, not much can be done besides maintaining dust-free chip surfaces and high-quality fabrication. It may be advisable to develop some manner of cleaning procedure for high-priority chips. The exact mechanisms behind thermal strain failures are not well understood. Some avenues for further investigation include the effects of cladding thickness and composition and the design of input nanotapers, since the damage is localized to the chip edge. If these concerns can be resolved, comb generation at 1.06 μm should be achievable in the near future.

REFERENCES

REFERENCES

[1] R. Holzwarth, T. Udem, and T. W. Hänsch, "Optical frequency synthesizer for precision spectroscopy," *Phys. Rev. Lett.*, vol. 85, no. 11, pp. 2264–2267, Sep. 2000.

[2] F. Riehle, "Optical clock networks," *Nature Photon.*, vol. 11, pp. 25–31, Jan. 2017.

[3] Y. J. Yan and S. Mukamel, "Femtosecond pump-probe spectroscopy of polyatomic molecules in condensed phases," pp. 6485–6504, Jun. 1990.

[4] C. B. Huang, Z. Jiang, D. Leaird, J. Caraquitena, and A. Weiner, "Spectral line-by-line shaping for optical and microwave arbitrary waveform generations," *Laser & Photon. Rev.*, vol. 2, no. 4, pp. 227–248, Apr. 2008.

[5] U. Keller, "Recent developments in compact ultrafast lasers," *Nature*, vol. 424, pp. 831–838, Aug. 2003.

[6] J. Levy, A. Gondarenko, M. Foster, A. Turner-Foster, A. Gaeta, and M. Lipson, "CMOS-compatible multiple-wavelength oscillator for on-chip optical interconnects," *Nature Photon.*, vol. 4, pp. 37–40, Dec. 2009.

[7] K. Saha, Y. Okawachi, J. Levy, R. Lau, K. Luke, M. Foster, M. Lipson, and A. Gaeta, "Broadband parametric frequency comb generation with a 1-μm pump source," *Opt. Express*, vol. 20, no. 24, pp. 26 935–26 941, Nov. 2012.

[8] T. J. Kippenberg, R. Holzwarth, and S. A. Diddams, "Microresonator-based optical frequency combs," *Science*, vol. 332, pp. 555–559, Apr. 2011.

[9] R. Wu, V. R. Supradeepa, C. Long, D. Leaird, and A. M. Weiner, "Generation of very flat optical frequency combs from continuous-wave lasers using cascaded intensity and phase modulators driven by tailored radio frequency waveforms," *Opt. Lett.*, vol. 35, no. 19, pp. 3234–3236, Oct. 2010.

[10] S. Yefet and A. Pe'er, "A review of cavity design for Kerr lens mode-locked solid-state lasers," *Appl. Sci.*, vol. 3, no. 4, pp. 694–724, Dec. 2013.

[11] L. Razzari, D. Duchesne, M. Ferrera, R. Morandotti, S. Chu, B. E. Little, and D. J. Moss, "CMOS-compatible integrated optical hyperparametric oscillator," *Nature Photon.*, vol. 4, pp. 41–45, Jan. 2010.

[12] J. Jaramillo-Villegas, X. Xue, P. H. Wang, D. Leaird, and A. M. Weiner, "Deterministic single soliton generation and compression in microring resonators avoiding the chaotic region," *Opt. Express*, vol. 23, no. 8, pp. 9618–9626, Apr. 2015.

[13] P. Del'Haye, A. Schliesser, O. Arcizet, T. Wilken, R. Holzwarth, and T. J. Kippenberg, "Optical frequency comb generation from a monolithic microresonator," *Nature*, vol. 450, pp. 1214–1217, Dec. 2007.

[14] S. Papp, P. Del'Haye, and S. Diddams, "Mechanical control of a microrod-resonator optical frequency comb," *Phys. Rev. X*, vol. 3, p. 031003, Jul. 2013.

[15] C. Y. Wang, T. Herr, P. Del'Haye, A. Schliesser, J. Hofer, R. Holzwarth, T. W. Hänsch, N. Picque, and T. J. Kippenberg, "Mid-infrared optical frequency combs at 2.5μm based on crystalline microresonators," *Nature Commun.*, vol. 4, p. 1345, Jan. 2013.

[16] A. Griffith, R. Lau, J. Cardenas, Y. Okawachi, A. Mohanty, R. Fain, Y. H. D. Lee, M. Yu, C. Phare, C. Poitras, A. Gaeta, and M. Lipson, "Silicon-chip mid-infrared frequency comb generation," *Nature Commun.*, vol. 6, p. 6299, Feb. 2015.

[17] K. Ikeda, R. Saperstein, N. Alic, and Y. Fainman, "Thermal and Kerr nonlinear properties of plasma-deposited silicon nitride/silicon dioxide waveguides," *Opt. Express*, vol. 16, no. 17, pp. 12 987–12 994, Aug. 2008.

[18] J. Bauer, "Optical properties, band gap, and surface roughness of Si_3N_4," *Phys. Stat. Sol. (a)*, vol. 39, pp. 411–418, Feb. 1977.

[19] A. M. Weiner, *Ultrafast Optics*. John Wiley & Sons, 2009.

[20] I. Agha, Y. Okawachi, and A. Gaeta, "Theoretical and experimental investigation of broadband cascaded four-wave mixing in high-Q microspheres," *Opt. Express*, vol. 17, no. 18, pp. 16 209–16 215, Aug. 2009.

[21] K. Luke, Y. Okawachi, M. Lamont, A. Gaeta, and M. Lipson, "Broadband mid-infrared frequency comb generation in a Si_3N_4 microresonator," *Opt. Lett.*, vol. 40, no. 21, pp. 4823–4826, Nov. 2015.

[22] G. Agrawal, *Nonlinear Fiber Optics*, 5th ed. Academic Press, 2012.

[23] M. Haelterman, S. Trillo, and S. Wabnitz, "Dissipative modulation instability in a nonlinear dispersive ring cavity," *Opt. Commun.*, vol. 91, pp. 401–407, Aug. 1992.

[24] T. Carmon, L. Yang, and K. Vahala, "Dynamical thermal behavior and thermal self-stability of microcavities," *Opt. Express*, vol. 12, no. 20, pp. 4742–4750, Oct. 2004.

[25] Y. Liu, Y. Xuan, X. Xue, P. H. Wang, S. Chen, A. Metcalf, J. Wang, D. Leaird, M. Qi, and A. Weiner, "Investigation of mode coupling in normal-dispersion silicon nitride microresonators for Kerr frequency comb generation," *Optica*, vol. 1, no. 3, pp. 137–144, Sep. 2014.

[26] X. Xue, M. Qi, and A. Weiner, "Normal-dispersion microresonator Kerr frequency combs," *Nanophotonics*, vol. 5, no. 2, pp. 244–262, Jun. 2016.

[27] W. D. Heiss and A. L. Sannino, "Avoided level crossing and exceptional points," *J. Phys. A*, vol. 23, pp. 1167–1178, 1990.

[28] I. Grudinin, L. Baumgartel, and N. Yu, "Impact of cavity spectrum on span in microresonator frequency combs," *Opt. Express*, vol. 21, no. 22, pp. 26 929–26 935, Nov. 2013.

[29] Y. Liu, Y. Xuan, X. Xue, P.-H. Wang, A. J. Metcalf, S. Chen, M. Qi, and A. M. Weiner, "Investigation of mode interaction in optical microresonators for Kerr frequency comb generation," in *CLEO: 2014*. Optical Society of America, 2014, p. FW1D.2.

[30] K. Luke, A. Dutt, C. Poitras, and M. Lipson, "Overcoming Si_3N_4 film stress limitations for high quality factor ring resonators," *Opt. Express*, vol. 21, no. 19, pp. 22 829–22 833, Sep. 2013.

[31] M. Rosenfield, M. Thomson, P. Coane, K. Kwietniak, and J. Keller, "Electron-beam lithography for advanced device prototyping: process tool metrology," *J. Vac. Sci. Technol. B*, vol. 11, p. 2615, Jul. 1993.

[32] Y. Xuan, Y. Liu, L. Varghese, A. Metcalf, X. Xue, P.-H. Wang, K. Han, J. Jaramillo-Villegas, A. A. Noman, C. Wang, S. Kim, M. Teng, Y. J. Lee, B. Niu, L. Fan, J. Wang, D. Leaird, A. Weiner, and M. Qi, "High-Q silicon nitride microresonators exhibiting low-power frequency comb initiation," *Optica*, vol. 3, no. 11, pp. 1171–1180, Nov. 2016.

[33] V. Almeida, R. Panepucci, and M. Lipson, "Nanotaper for compact mode conversion," *Opt. Lett.*, vol. 28, no. 15, pp. 1302–1304, Aug. 2003.

[34] P. H. Wang, "On-chip microresonator frequency combs: Generation dynamics, power transfer, and time-domain characterization," Ph.D. dissertation, Purdue University, May 2016.

[35] A. Al-Norman, "Optical characterization of on-chip silicon nitride microresonators," Master's thesis, Purdue University, May 2016.

[36] R. Morgan, J. Barton, P. Harper, and J. Jones, "Wavelength dependence of bending loss in monomode optical fibers: effect of the fiber buffer coating," *Opt. Lett.*, vol. 15, no. 17, pp. 947–949, Sep. 1990.

[37] J. Bauters, M. Heck, D. John, D. Dai, M. C. Tien, J. Barton, A. Leinse, R. Heideman, D. Blumenthal, and J. Bowers, "Ultra-low-loss high-aspect-ratio Si_3N_4 waveguides," *Opt. Express*, vol. 19, no. 4, pp. 3163–3174, Feb. 2011.

[38] A. Fallahkhair, K. Li, and T. Murphy, "Vector finite difference modesolver for anisotropic dielectric waveguides," *J. Lightwave Technol.*, vol. 26, no. 11, pp. 1423–1431, Jun. 2008. [Online]. Available: https://www.photonics.umd.edu/software/wgmodes/

[39] W. Lui, T. Hirono, K. Yokoyama, and W. P. Huang, "Polarization rotation in semiconductor bending waveguides: A coupled-mode theory formulation," *J. Lightwave Technol.*, vol. 16, no. 5, pp. 929–936, May 1998.

[40] S. Ramelow, A. Farsi, S. Clemmen, J. Levy, A. Johnson, Y. Okawachi, M. Lamont, M. Lipson, and A. Gaeta, "Strong polarization mode coupling in microresonators," *Opt. Lett.*, vol. 39, no. 17, pp. 5134–5137, Sep. 2014.

[41] S. Xiao, M. Khan, H. Shen, and M. Qi, "Modeling and measurement of losses in silicon-on-insulator resonators and bends," *Opt. Express*, vol. 15, no. 17, pp. 10 553–10 561, Aug. 2007.

[42] X. Xue, Y. Xuan, Y. Liu, P. H. Wang, S. Chen, J. Wang, D. Leaird, M. Qi, and A. Weiner, "Mode-locked dark pulse Kerr combs in normal-dispersion microresonators," *Nature Photon.*, vol. 9, pp. 594–600, Aug. 2015.

[43] Q. Li, A. Eftekhar, M. Sodagar, Z. Xia, A. Atabaki, and A. Adibi, "Vertical integration of high-Q silicon nitride microresonators into silicon-on-insulator platform," *Opt. Express*, vol. 21, no. 15, pp. 18 236–18 248, Jul. 2013.

[44] R. Kashyap, "The fiber fuse - from a curious effect to a critical issue: A 25th year retrospective," *Opt. Express*, vol. 21, no. 5, pp. 6422–6441, Mar. 2013.

[45] R. Kashyap, B. Ainslie, and G. Maxwell, "Second-harmonic generation in a GeO_2 ridge waveguide," *Electron. Lett.*, vol. 25, no. 3, pp. 206–208, Feb. 1989.

[46] A. M. Weiner, "Femtosecond pulse shaping using spatial light modulators," *Rev. Sci. Instr.*, vol. 71, no. 5, pp. 1929–1960, May 2000.

[47] R. Nelson, D. Leaird, and A. Weiner, "Programmable polarization-independent spectral phase compensation and pulse shaping," *Opt. Express*, vol. 11, no. 15, pp. 1763–1769, Jul. 2003.

[48] R. Thurston, J. Heritage, A. Weiner, and W. Tomlinson, "Analysis of picosecond pulse shape synthesis by spectral masking in a grating pulse compressor," *IEEE J. Quantum Electron.*, vol. 22, no. 5, pp. 682–696, May 1986.

[49] M. Teng, B. Niu, K. Han, and M. Qi, "Effect of waveguide surface roughness on the fiber coupling efficiency of inverse tapers," in *Optical Fiber Communication Conference*. Optical Society of America, 2015, p. Th3F.6.

APPENDICES

A. EXAMPLE DEVICES

Table A.1-2 list some examples of specific devices characterized over the course of this project. The first eight contain mode interactions in the wavelength range of interest (1055-1070 nm). These received the greatest amount of attention due to their potential to generate normal-dispersion combs. Unfortunately all known channels with mode interactions in the target range have been damaged. The ninth and tenth (both from Purdue160707_A1), were part of an early attempt at dispersion engineering. Most devices, however, were set aside after the initial transmission scan due to lack of mode interactions, low Qs, or poor coupling. Nonetheless, they can provide useful information to help guide device design. The last three chips fall into this category. Four devices from the table are described in greater detail below.

All the below chips were tested before the pump blocker came online. Threshold power is calculated assuming under-coupling, and simulated values are for the fundamental TE mode. Several broad trends emerge from these data. First, narrower waveguides tend to be associated with lower Qs, especially below $W = 1$ μm. However, there is still significant variation from chip to chip due to fabrication quality and other design choices. Intrinsic Qs above 2 million are rare at 1 micron, and so far no devices with Q_0 above 3 million have been observed. In contrast, some devices with Q_0 in excess of 10 million have been reported at 1.5 microns.

As expected, wider waveguides support more transverse modes, although $H = 300$ nm chips can sometimes support fewer modes than expected. Devices with FSRs on the order of 50 GHz are overrepresented in the list of chips with mode interactions, but tend to have expected threshold powers that put them at high risk of damage. An FSR on the order of 100 GHz seems to be the ideal compromise for achieving a good probability of mode interactions while maintaining reasonable threshold powers.

Table A.1.
Selected devices

Device	Height x Width (nm)	FSR (GHz)	Modes	Sim. A_{eff} (μm^2)	Sim. D (ps/nm-km)	Extinct. Rat. (dB)	Q_i
Purdue160222_A4_Ch1	300x3000	49	3	0.97	-660	14	1.3 M
Purdue160222_A4_Ch3	300x3000	49	3	0.97	-660	8.5	2.0 M
ND160315_A2_Ch1	600x2000	48	2	0.85	-75	2.0	2.0 M
ND160315_A12_Ch2	600x2000	49	2	0.85	-75	15	1.2 M
ND160315_A12_Ch3	600x3000	49	3	1.25	-120	14	1.5 M
Purdue160603_A1_Ch6	740x2000	48	2	0.97	-30	3.5	2.2 M
Purdue160925_A2_Ch3	300x2000	137	1	0.67	-630	11	1.5 M
Purdue1612_D4_23	770x2000	99	2	1.0	-25	1.5	1.8 M
Purdue160707_A1_Ch1	580x1000	222	1	0.47	12	5.0	0.25 M
Purdue160707_A1_Ch7	580x1500	370	2	0.65	-45	6.0	0.75 M
Purdue160202_A1_Ch1	300x2000	35	2	0.67	-630	8.5	2.0 M
Purdue160925_A1_Ch2	300x1300	137	1	0.47	-620	7.0	0.9 M
ND160315_A12_Ch5	600x2000	99	1	0.85	-75	12	1.1 M

Table A.2.
Selected devices (Continued)

Device	Loss/ Facet (dB)	Calc. P_{th} (mW)	Interaction	Damage
Purdue160222_A4_Ch1	1.8	240	1062 nm	Y
Purdue160222_A4_Ch3	1.8	80	1061 nm	Y (200 mW)
ND160315_A2_Ch1	2.5	110	1062 nm	Y
ND160315_A12_Ch2	2.5	180	1059 nm	Y
ND160315_A12_Ch3	2.5	120	1068 nm	Y
Purdue160603_A1_Ch6	3.0	100	1058 nm	Y (250 mW)
Purdue160925_A2_Ch3	2.5	50	1065 nm	Y (250 mW)
Purdue1612_D4_73	3.5	65	1058 nm	Y (160 mW)
Purdue160707_A1_Ch1	3.0	480	None	Y (200 mW)
Purdue160707_A1_Ch7	3.0	60	None	N
Purdue160202_A1_Ch1	2.5	90	None	N
Purdue160925_A1_Ch2	2.5	130	None	N
ND160315_A12_Ch5	2.5	110	None	N

A.1 Purdue160222_A4_Ch3

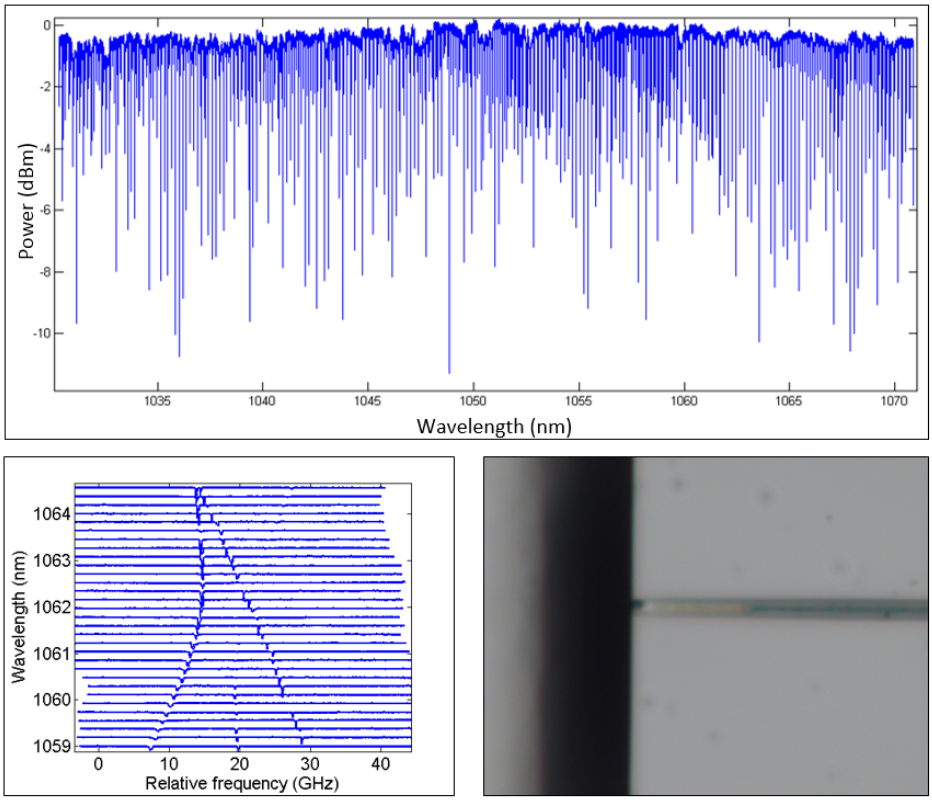

Fig. A.1. **(a)** Transmission spectrum of Purdue160222_A4_Ch3. **(b)** Mode interaction at 1061 nm. The modes from left to right along the bottom of the plot are TE1, TE2, and TE3. **(c)** Fiber fuse damage at input facet; silicon nitride taper destroyed.

This device, the second in Table A.1, was one of the first high-Q resonators found at 1 micron. Like most 3000 nm-wide waveguides, it can support three transverse modes: TE1-3 with FSR of 49.6 GHz, 49.3 GHz, and 48.6 GHz respectively. TE1 and TE2 can be seen interacting strongly at 1061 nm, while TE3 displays no coupling with either of the others (Figure A.1). As is expected for a 300 nm thickness, the fundamental mode displays strong normal dispersion, with a measured value of -800 ps/nm-km and a simulated value of -660 ps/nm-km.

This device and the other from the same chip are notable for their low insertion loss, approximately 1.8 dB per facet. This loss is affected by fabrication quality and the dimensions of the inverse taper, though the latter effect has not be studied in detail at 1 micron. However, the tapers used have lengths of 45 μm and tip widths of 170 nm, which is near the theoretical optimum for 1.5 μm [49]. In contrast, the fabrications on 16/07/07 and 16/09/25 used 30 μm by 300 nm tapers and achieved more typical losses of 2.5-3.0 dB per facet.

With a resonator-bus gap size of 400 nm, the ring is predicted to be moderately under-coupled. This and its intrinsic Q of 2.0 million give it an expected threshold power of 80 mW. Unfortunately, too much power was used in probing for combs, and this channel became the project's first example of the fiber fuse effect. This occurred at an input power of 200 mW, or 130 mW in the bus waveguide after accounting for insertion loss.

A.2 Purdue1612_D4_23

This device was created as part of our group's project seeking to assemble a SiN comb generator with InP integrated optics, and as such has angled bus waveguides to minimize back-reflection between the different components. To maximize transmission, the lensed fiber should be set at an angle of about 21° to the bus (Figure A.2). The film thickness is 770 nm, and although simulation predicts a normal dispersion of -25 ps/nm-km, experimental measurements are unable to rule out anomalous dispersion. The device also has a weak mode interaction at 1058 nm.

Although the device has very low extinction at 1.5 dB, its intrinsic Q of 1.8 million is high enough to give it a threshold power of only 65 mW. Unfortunately, its thick waveguides also made it especially susceptible to thermal strain damage, and it failed at 160 mW without showing any evidence of comb generation. Due to the increased insertion loss of 3.5 dB per facet often seen in angled-waveguide chips, this implied a power of 70 mW in the bus waveguide.

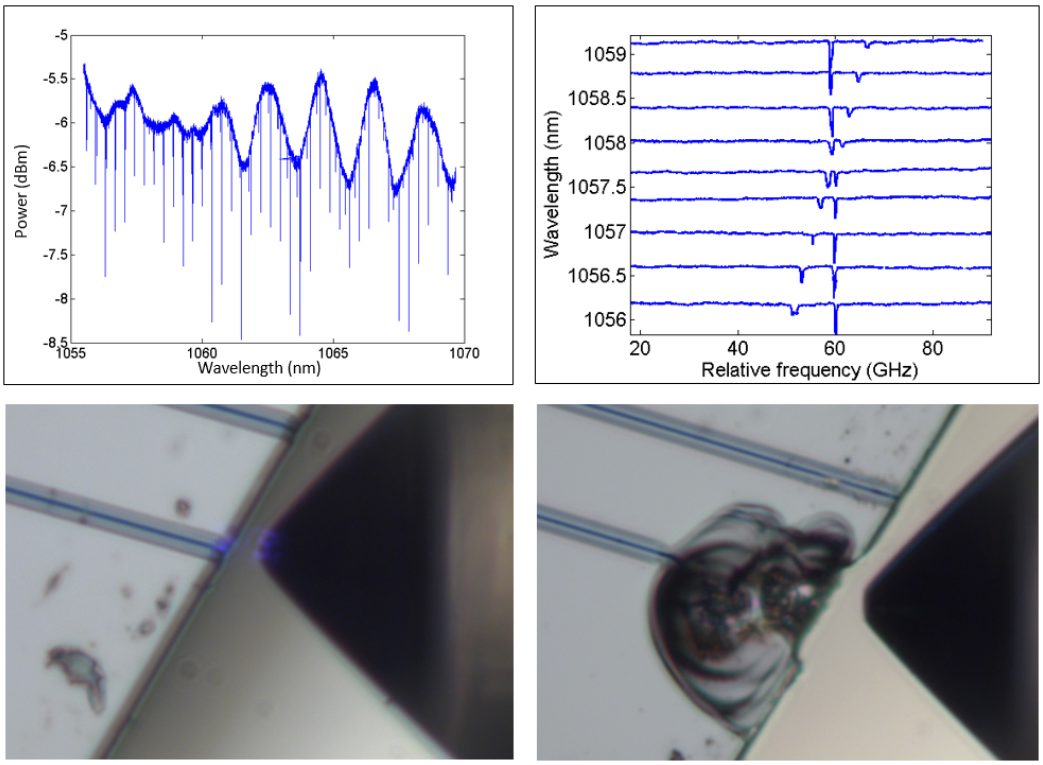

Fig. A.2. **(a)** Transmission spectrum of Purdue1612_D4_23. **(b)** Weak mode interaction at 1058 nm. The modes from left to right along the bottom of the plot are TE1 and TE2. **(c)** Lensed fiber at 21° relative to waveguide. Blue light in coupling area thought to be an artifact of video microscope's CCD. **(d)** Thermal strain damage to input facet.

A.3 Purdue160707_A1_Ch1

This device was part of an early effort toward dispersion engineering dispersion. Given waveguide dimensions of 580x1000 nm, simulation predicts a weak anomalous dispersion of 12 ps/nm-km. However, experimental measurements gave a value of -140 ps/nm-km (though this comes with a significant margin of error). The narrowness of the resonator waveguide also significantly increased loss, leading to an intrinsic Q of 250,000 and a threshold power of 480 mW.

High power testing was nevertheless attempted. No evidence of comb generation was found, and the channel suffered a thermal strain failure at approximately 200

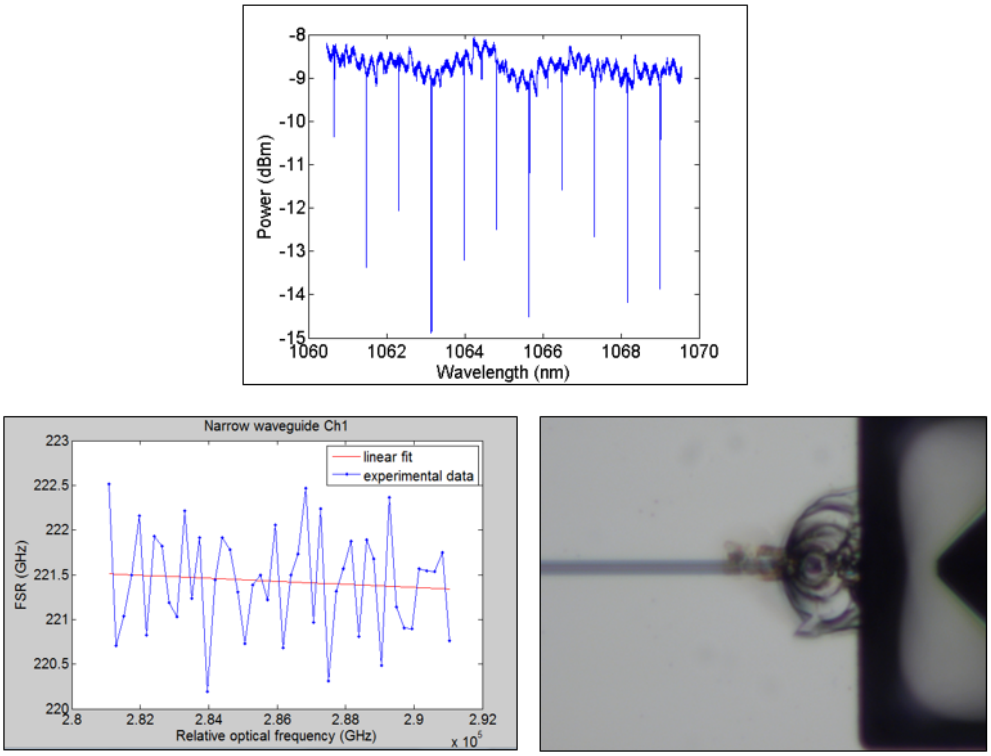

Fig. A.3. **(a)** Transmission spectrum of Purdue160707_A1_Ch1. **(b)** Fit of FSR evolution for dispersion measurement. **(c)** Thermal strain damage to input facet.

mW, or 110 mW in the bus (Figure A.3). It is possible that the low Qs seen on this chip were in part due to a bad fabrication batch, but nonetheless the decision was made at this point to focus on normal dispersion combs.

A.4 Purdue160202_A1_Ch1

This was one of the lowest-FSR devices I tested. Generally, large ring circumference leads to higher threshold powers, but this resonator's high Q_0 of 2.0 million and nearly ideal coupling parameter of $K = 0.42$ gives it an expected threshold of 90 mW (Figure A.4. Unfortunately, its two modes never experience coupling over the 15 nm range of interest, and its waveguide dimensions of 300x2000 nm put it solidly in the normal dispersion regime, with a simulated D = -630 ps/nm-km. This underscores

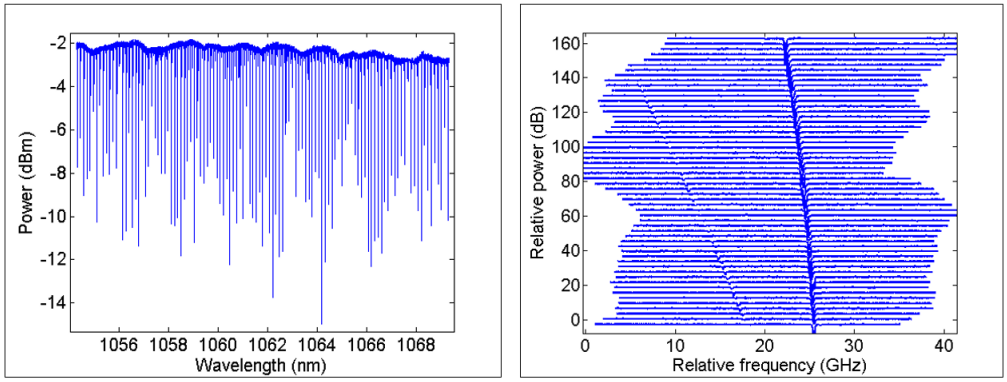

Fig. A.4. **(a)** Transmission spectrum of Purdue160202_A1_Ch1. **(b)** No mode coupling over range of interest.

an important point about normal-dispersion comb generation: good design can tilt the odds in your favor, but chance will always play a role.